Check for updates

ENGINEERING

Unveiling the fundamentals of flow boiling heat transfer enhancement on structured surfaces

Mohammad Jalal Inanlu[1], Vishwanath Ganesan[1], Nithin Vinod Upot[1], Chi Wang[1], Zan Suo[1], Kazi Fazle Rabbi[1], Pouya Kabirzadeh[1], Alireza Bakhshi[1], Wuchen Fu[1], Tarandeep Singh Thukral[1], Valentin Belosludtsev[1], Jiaqi Li[1,2]*, Nenad Miljkovic[1,3,4,5,6]*

Copyright © 2024 The Authors, some rights reserved; exclusive licensee American Association for the Advancement of Science. No claim to original U.S. Government Works. Distributed under a Creative Commons Attribution NonCommercial License 4.0 (CC BY-NC).

Micro- and nanostructured surfaces offer the potential to enhance two-phase heat transfer. However, the mechanisms behind these enhancements are not well-understood due to insufficient diagnostic methods, leading to reliance on trial-and-error surface development. We introduce in situ boroscopy to investigate microscale bubble dynamics during flow boiling nucleation and subsequent flow regime development. This method was applied in saturated flow boiling experiments within chemically etched aluminum and copper tubes. Although the surfaces have self-similar surface structures, our findings revealed varied heat transfer coefficient enhancements, with increases of up to 391% on aluminum and 41% on copper. Using boroscopy, we identified key mechanisms of heat transfer enhancement. We further used mercury porosimetry to determine the impact of pore size distribution on thermal performance. The boroscopy technique introduced here not only elucidates the underlying processes of flow boiling heat transfer enhancement but also has potential applications for the study of other two-phase phenomena.

INTRODUCTION

The increased demand for societal decarbonization and the consequent need for electrification have created a major need for efficient and powerful thermal management approaches and system architectures. Thermal management methods that use the latent heat of the working fluid for phase change hold a notable advantage over other cooling schemes due to their high energy density and relatively constant streamwise temperature. Hence, two-phase cooling schemes like flow boiling are widely used in many industries including electronics (*1*), transportation thermal management (*2*), air conditioning and refrigeration (*3*), power generation (*4*), and space applications (*5*).

Flow boiling performance is commonly evaluated using two parameters: the heat transfer coefficient (HTC) and the maximum allowable heat flux, also called critical heat flux (CHF). The CHF is typically the more critical parameter of the two, leading to either departure from nucleate boiling (at high subcooling, high mass flux, and high wall heat flux) or dryout of the surface (in the opposing case: low subcooling, low mass flux, and low heat flux) (*6*). The HTC is defined as the ratio of the amount of heat transferred per unit time per unit area to the temperature difference between the heated surface and the bulk surrounding fluid. Departure from nucleate boiling occurs when bubbles cannot reach the liquid due to strong core condensation forming a vapor blanket, blocking liquid flow to the wall, and causing a rapid rise in wall temperature. Dryout occurs when the heat flux is high enough (CHF) for the vapor generated at the hot surface to induce a dewetting instability, leading to a partial or complete depletion of the liquid film wetting the heated surface. This dryout phenomenon similarly causes a rapid increase in wall temperature due to poor heat transfer properties of vapor as compared to liquid and thus causes a decrease in HTC, leading to overheating and potential damage to the system. Researchers have been striving to enhance flow boiling performance for several decades by systematically improving these two fundamental parameters of HTC and CHF (*7*). These efforts include the use of microscale features such as micropillar arrays (*8*), microporous coatings (*9*), and artificial microcavities (*10*); nanoscale features such as copper (*11*) or silicon (*12*) nanowires, copper oxide nano blades (*13*), and carbon nanotubes on microchannels (*14*), mini channels (*15*), or silicon wafers (*16*); and methods with both micro and nanoscale structures (*17*, *18*).

Although the literature is rife with methods to enhance heat transfer performance through surface modification, there remains a poor understanding of the underlying enhancement mechanisms and their relationship to surface characteristics (*19*–*22*). Argumentations and hypotheses are understood and proposed mainly based on indirect observations using industrially irrelevant geometries and materials such as polished silicon wafers and planar bonded architectures (*23*, *24*). Few have attempted to conduct direct visualization of flow boiling on industrially relevant materials using geometries of proper design such as metallic tubes and channels (*25*, *26*). As a matter of convenience, most studies focus on pool boiling (*27*), predominantly using side-view visualization (*28*), and are mostly limited to atmospheric pressure conditions using convenient working fluids such as water. However, refrigerants have bubble nucleation and departure sizes that are up to two orders of magnitude smaller than those observed in water. These bubbles have radii that are <50 μm, smaller than the thickness of human hair (*29*), necessitating the need for the development of high-magnification and high-resolution visualization techniques.

When considering the flow boiling process, direct observation becomes even more challenging. Previous efforts have primarily been limited to experiments in microchannels using adiabatic glass covers (*30*, *31*). However, for two-phase flow boiling in round tubes, which is widely relevant for industrial applications, the underlying

[1]Department of Mechanical Science and Engineering, University of Illinois, Urbana, IL 61801, USA. [2]School of Energy and Power Engineering, Nanjing University of Science and Technology, Nanjing 210094, China. [3]Department of Electrical and Computer Engineering, University of Illinois, Urbana, IL 61801, USA. [4]Materials Research Laboratory, University of Illinois, Urbana, IL 61801, USA. [5]International Institute for Carbon Neutral Energy Research (WPI-I2CNER), Kyushu University, 744 Moto-oka Nishi-ku, Fukuoka 819-0395, Japan. [6]Institute for Sustainability, Energy and Environment (iSEE), University of Illinois at Urbana-Champaign, Urbana, 61801 IL, USA.
*Corresponding author. Email: nmiljkov@illinois.edu (N.M.); lijiaqi@njust.edu.cn (J.L.)

Downloaded from https://www.science.org at EPF Lausanne on October 12, 2025

physical mechanisms notably differ from those observed in microchannels due to different thermo-fluidic phenomena governing the bubble-dominated boundary layer near the surface as well as bulk flow fluid dynamics. Moreover, the adiabatic nature of the glass sections drastically alters the heating conditions, thus undermining the relevance of the results. Hence, without an effective method for direct visualization, the current state of the field relies on trial-and-error methods to develop structured surface designs for flow boiling heat transfer enhancement. Furthermore, global decarbonization efforts have led to the development and implementation mandates of emerging synthetic refrigerant blends with low global warming potential (GWP) and low ozone depletion potential (ODP) which are both difficult to work with and understand from a two-phase heat transfer perspective. These knowledge gaps highlight the need for a non-intrusive approach to observe and study the mechanisms of heat transfer enhancement during flow boiling on structured surfaces.

Building on our prior work using boroscopy to investigate the fundamental mechanisms governing pool boiling (*32*, *33*), we have adapted this technology to uncover the mechanisms driving flow boiling on structured surfaces. We observed that different etching chemistries (resulting in different structure sizes) can result in wildly different levels of heat transfer enhancement (*18*, *34*, *35*). However, without effective direct in situ visualizations, it is impossible to accurately identify the factors influencing the observed differences in structures of various sizes used for flow boiling. In this study, we shed light on the role that surface structures play on the flow boiling performance of the low-GWP, low-ODP refrigerant R515B using high-magnification in situ and in-liquid boroscopy. By integrating boroscopy with systematic flow boiling experiments, we demonstrate the ability to observe and study in situ bubble nucleation dynamics, bubble growth, bubble departure, the subsequent flow regime transitions, and dryout dynamics; offering critical insights that are paramount to the advancement of thermal management technologies. By using high-speed and high-magnification imaging with spatial resolutions as fine as 5 μm per pixel, we provide a comprehensive understanding of how surface modifications having micro- to nano-length scales drive heat transfer enhancement. Our insights offer a comprehensive understanding of the nuanced flow boiling process and provide design guidelines for scientists and engineers to help tailor surface features for ideal performance.

RESULTS AND DISCUSSION

Surface characterization

To understand the role that surface structures play on flow boiling heat transfer and to establish a platform for boroscopy, we use two etch chemistries that can create distinct surface structures having distinct length scales: an aluminum (Al) tube of inner diameter 4.57 mm etched in a rapid reaction with quiescent hydrochloric acid (HCl) for 15 min and a copper (Cu) tube of inner diameter 4.72 mm etched in a slower and more passive reaction with ferric chloride ($FeCl_3$) for 20 min (HCl does not etch Cu). See Materials and Methods, text S1, and table S1 for further micro- and nanofabrication details. The Al and Cu materials were chosen because of their common use in energy applications (*3*). The etch chemistries were developed to be highly scalable and low cost (*18*, *34*–*37*) and were rationally chosen because of their formation of cavities and roughness features on the metal surfaces that are self-similar.

Figure 1 illustrates the morphological differences between the plain and etched Al and the plain and etched Cu samples. Using scanning electron microscopy (SEM; see Materials and Methods), focused ion beam (FIB) milling aided cross-sectional SEM (see Materials and Methods), and x-ray photoelectron spectroscopy (XPS; see Materials and Methods) analyses, we establish both topographical and chemical understanding of the surfaces. The images reveal that the etching process creates distinct surface features on the metal samples which appear to have similar length scales (at the nanoscale level). Figure 1 (D, E, J, and K), alongside their insets, shows the presence of nanoscale structures and more cavities on both the etched Al and etched Cu surfaces. In comparison to the structured etched samples, the unstructured surfaces consisting of plain Al and plain Cu samples (Fig. 1, A, B, G, and H) show fewer cavities. The chemical state of the surfaces is shown in Fig. 1 (C, F, I, and L) using wide-band XPS spectra. Figure 1C illustrates various additional elements present on the plain Al tube stemming from the manufacturing process of the alloy (Al6061). However, these elements are eliminated after etching, leaving only Al and O (Fig. 1F). The wide-band XPS spectra of Al 2p and O 1s confirm the existence of Al and O on the etched surface, with peaks at the anticipated binding energies. The inset of Fig. 1F shows higher-resolution spectra that demonstrate the metal and oxide peaks, further corroborating the existence of Al and O. In contrast, Fig. 1I shows the presence of only Cu and O on the plain Cu tube, and the spectra remain largely unchanged (Fig. 1L) after etching. The wide-band XPS spectra of Cu 2p and O 1s (also visible in the inset in further detail) confirm the existence of Cu and O on the etched surface, with peaks at the expected binding energies. These observations prove the existence of CuO on the surface.

Heat transfer performance

To test the heat transfer performance of our surfaces, we used a custom-built flow boiling setup (Fig. 2A; see Materials and Methods). Details of the HTC enhancements, pressure drop quantification, and their response to varying heat flux and mass flux are presented in text S2 and fig. S1. In short, experiments were carried out for three different mass fluxes of $G = 100$, 150, 200 kg/(m^2·s) for plain and etched Al surfaces, representing the primary focus of the investigation. To further establish a basis for comparing the impact of surface structural variations on HTC, additional experiments were performed on plain and etched Cu surfaces at a mass flux of $G = 150$ kg/(m^2·s). Comparing results on plain and etched Al surfaces, at low mass flux of $G = 100$ kg/(m^2·s), an increase of maximum HTC averaged over the heated tube length as high as 391% is measured pre-CHF on the etched Al surface when compared to the plain Al surface (see text S2). The heat transfer enhancement reduced with increasing mass flux due to the suppression of nucleate boiling (*38*) [with maximum enhancement in HTC averaged over the heated tube length up to 191% for $G = 150$ kg/(m^2·s) and up to 181% for $G = 200$ kg/(m^2·s); see text S2]. Contrary to the etched Al surface, lower levels of enhancement in HTC averaged over the heated tube length were observed with the etched Cu surface, reaching only up to only 41% for $G = 150$ kg/(m^2·s). In the main text, we focus on the case of $G = 150$ kg/(m^2·s), while the results for the remaining mass fluxes are discussed in detail in the Supplementary Materials. Comparing the HTC measurements at different axial locations along the tube reveals that our structured surfaces primarily enhance nucleate boiling (*35*). In a broader context, HTC enhancements with surface structures have been shown to be more dominant during nucleate

Downloaded from https://www.science.org at EPF Lausanne on October 12, 2025

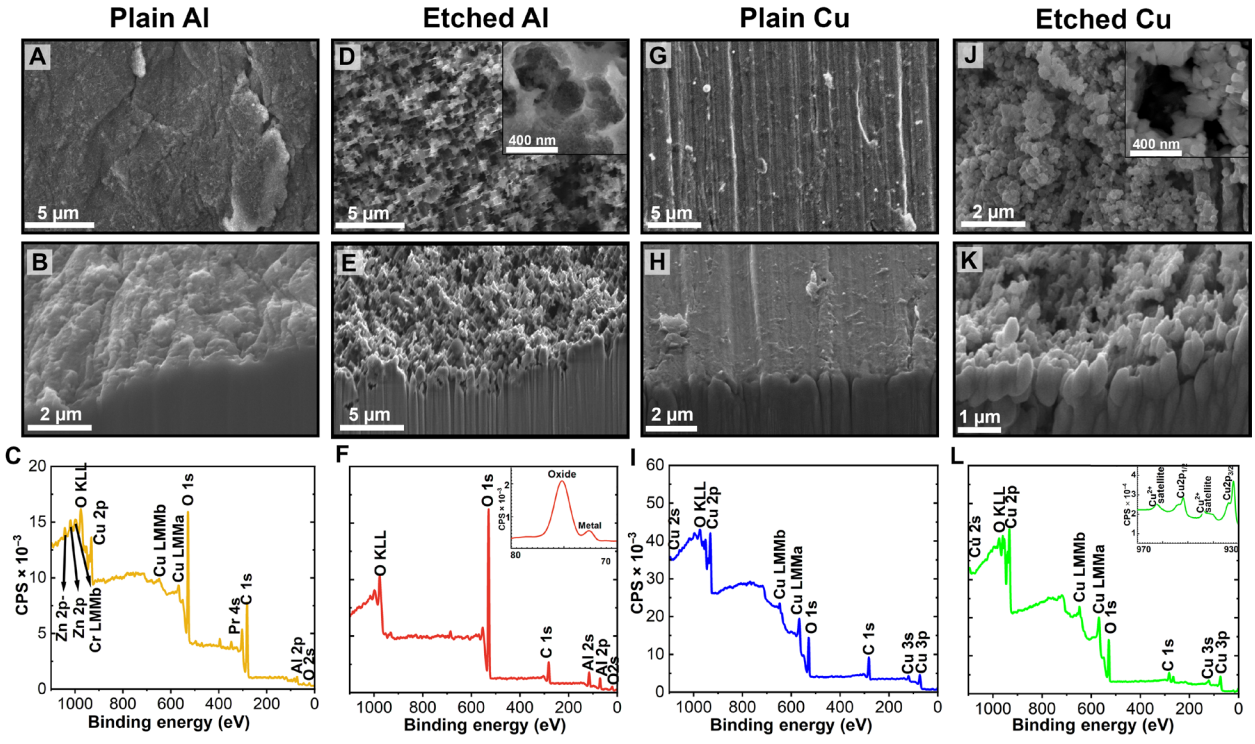

Fig. 1. Comparative analysis for different surfaces under study via SEM, FIB, and XPS techniques. SEM, FIB-aided cross-sectional SEM, and XPS images for (**A** to **C**) plain Al, (**D** to **F**) etched Al, (**G** to **I**) plain Cu, and (**J** to **L**) etched Cu. SEM images clearly display the existence of nanoscale cavities on etched surfaces, while these features are notably absent on smooth plain surfaces. XPS images of plain Al display various surface elements, removed by etching, leaving only Al and O. Chemically, the Cu surface remains mostly unchanged after etching, with the presence of Cu metal and CuO.

boiling within the bubbly flow regime when compared to convective boiling within the annular flow regime (*39*), and the ratio of maximum HTCs in these two distinct heat transfer modes could be as high as ~2.5 times (*35*). Thus, we mainly focus on the dominant heat transfer mode of nucleate boiling and its associated mechanisms that surface structures use to enhance heat transfer. Furthermore, we conducted additional experiments to identify all intermediary flow regimes during saturated boiling by carrying out visualization at different spatial locations along the tube axis. These efforts were aimed at investigating the potential effects of these structures on actual quality (x), flow regime transitions, and dryout type CHF phenomenon. It is important to note that the actual quality is the ratio of the vapor mass flow rate to the total mass flow rate which is not necessarily the same as thermodynamic equilibrium quality, x_e, that is derived from energy balance at any axial location z from the tube inlet: $x_{e,z} = x_{e,in} + (4q''/Gh_{fg})(z/D)$. Here, q'' is the uniform wall heat flux applied along the tube of inner diameter D, h_{fg} is the latent heat of vaporization of the working fluid, and $x_{e,in}$ is the inlet thermodynamic equilibrium quality. Thermodynamic equilibrium quality serves as the maximum theoretical limit for actual quality during saturated flow boiling with the liquid and vapor phases under thermal equilibrium. In other words, at any given location within the saturated flow boiling regime, actual quality is mostly lower than the thermodynamic equilibrium quality as in reality, instead of having vapor bubbles (at temperature T_g) in thermal equilibrium with the bulk fluid (at saturation temperature T_{sat}), a fraction of the applied wall heat flux is often used to superheat the vapor bubbles ($\Delta T_g = T_g - T_{sat} > 0$) departing from the surface.

Boroscopy enabled bubble dynamics analysis: Aluminum

To obtain a better understanding of the enhancement mechanisms with respect to different flow regimes, we used two, state-of-the-art borescopes (MicroSlim and Pro Hardy; see Materials and Methods) inserted near the entrance (Mirco Slim, 2% of the axial length) as shown in Fig. 2 (B and D), at 30% of the axial length (Pro Hardy) as shown in Fig. 2 (C and E), and near the exit (Pro Hardy, 95% of the axial length) as shown in Fig. 2 (C and F) of any given tube sample. Figure 3A shows boroscopy imaging results for the plain and etched Al surfaces at $G = 150$ kg/(m^2·s) where the borescope is inserted near the entrance (2% axial length) of the tube. In this context, distinct cases are classified on the basis of their tube exit thermodynamic equilibrium qualities ($x_{e,out}$), which were made to be consistent across all tubes within each case (see Materials and Methods). For a fixed inlet thermodynamic equilibrium quality ($x_{e,in} = 0$) under saturated liquid inlet conditions, fixing the exit thermodynamic equilibrium qualities for distinct cases also automatically fixes the local thermodynamic equilibrium qualities ($x_{e,z}$) for those cases as witnessed from the following linear variation of $x_{e,z} = (4q''/Gh_{fg})(z/D)$ with axial location. It is observed that, near the entrance, the etched Al surface with many more active nucleation sites (Fig. 3, A and D) results in a larger quantity of bubbles with smaller sizes when compared to the plain Al surface. The abundance of active nucleation sites on the etched Al surface aids in better heat removal via boiling heat transfer thus reducing the wall superheat (*40*) (shown in Fig. 3B) that ultimately results in the HTC enhancements (HTC $\propto 1/\Delta T_{sat}$) as depicted in Fig. 3C showing the local HTC at 2% of the axial length. On average, an increase of 211% was observed

Downloaded from https://www.science.org at EPF Lausanne on October 12, 2025

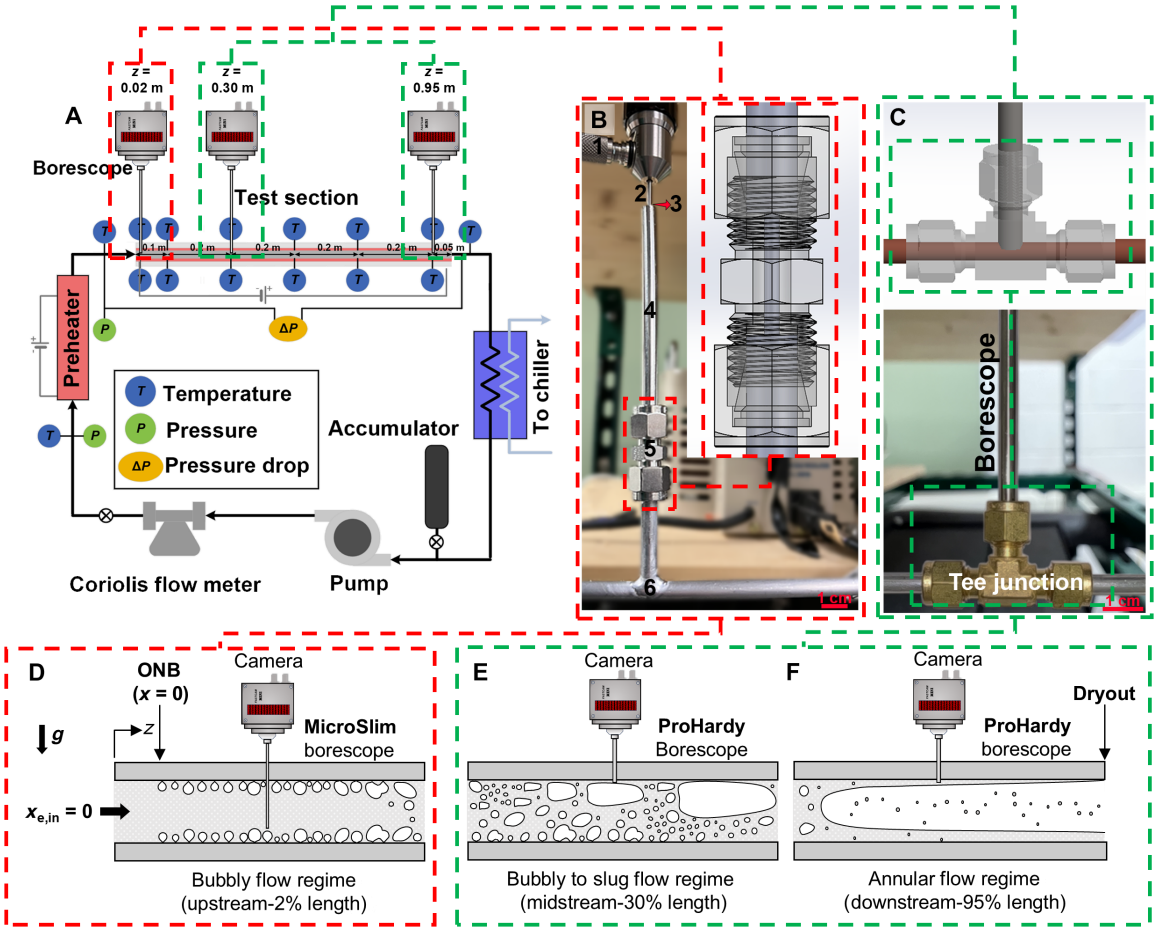

Fig. 2. Borescope imaging configurations and schematic of the setup. (**A**) Schematic of the setup representing the locations of borescope insertion, temperature sensors, pressure sensors, and other main components (see Materials and Methods). (**B**) MicroSlim borescope imaging configuration for the study of nucleation (1: fiber-optic cable for lighting, 2: borescope main probe, 3: epoxy seal, 4: auxiliary probe for sealing, 5: compression fitting, and 6: welded secondary tube). (**C**) Pro Hardy borescope imaging configuration for the study of bubbly/slug/plug and annular flow. (**D**) Schematic of the MicroSlim borescope imaging configuration for the study of bubble nucleation. MicroSlim borescope was used for the study of nucleation (inserted at $z = 0.02$ m) as higher resolutions were required to capture the microscale physics. Schematic of Pro Hardy borescope imaging configuration for the study of (**E**) bubbly/slug/plug flow regime (inserted at $z = 0.3$ m) and (**F**) annular flow regime (inserted at $z = 0.95$ m). $x_{e,in}$ is the inlet thermodynamic equilibrium quality which is set to zero (saturated liquid inlet conditions). Schematics not to the scale.

for the local HTC over different wall heat fluxes, with the enhancement increasing with increasing heat flux (up to 268%) due to the activation of additional nucleation sites at higher heat fluxes (seen in Fig. 3D) (*41*).

Figure 3 (D to G) analyzes boroscopy imaging results for plain and etched Al surfaces. The results show that with increasing heat flux, the bubble departure frequency and departure diameter for both plain and etched surfaces increase, in agreement with previously hypothesized mechanisms for refrigerant flow boiling on plain surfaces (*29*). The etched Al surface shows a higher active nucleation site density (N_a), smaller average bubble departure diameter (d_b), lower average bubble departure frequency (f), and a slower average bubble growth rate (dr/dt) before departure, when compared to the plain Al surface. While the higher nucleation site density is the result of more cavities created by the etching process which can be seen from the surface topography (Fig. 1), the differences in the bubble growth rate, departure diameter, and frequency are mainly caused by differences in wall superheat (difference between wall temperature and saturation temperature, $\Delta T_{sat} = T_w - T_{sat}$; Fig. 3B) as well as differences in surface wettability between the plain and etched surfaces (see text S3, fig. S2, and table S2). It is noteworthy that the departed bubble sizes visible in Fig. 3A may not accurately reflect the diameter at the departure; they are isolated, unmerged bubbles but not necessarily immediately after departure. Bubbles undergo superheating near the surface through microlayer evaporation, and as they grow and interact with the surrounding saturated liquid away from the surface, they will further undergo macrolayer evaporation, leading to their further expansion. Also, one should bear in mind that, although on the same surface, nucleation sites with smaller bubble departure diameters result in higher departure frequencies, comparing two distinct surfaces for which wall superheat and wettability are completely different is more challenging. This is observed for the etched Al surface which showed both a smaller average bubble departure diameter and lower average departure frequency as compared to the plain Al surface.

Figure 3G shows that the average bubble departure diameter (d_b) is lower on the etched Al surface, which is due to both the reduced local wall superheat (ΔT_{sat}) as shown in Fig. 3B and due to the highly

Downloaded from https://www.science.org at EPF Lausanne on October 12, 2025

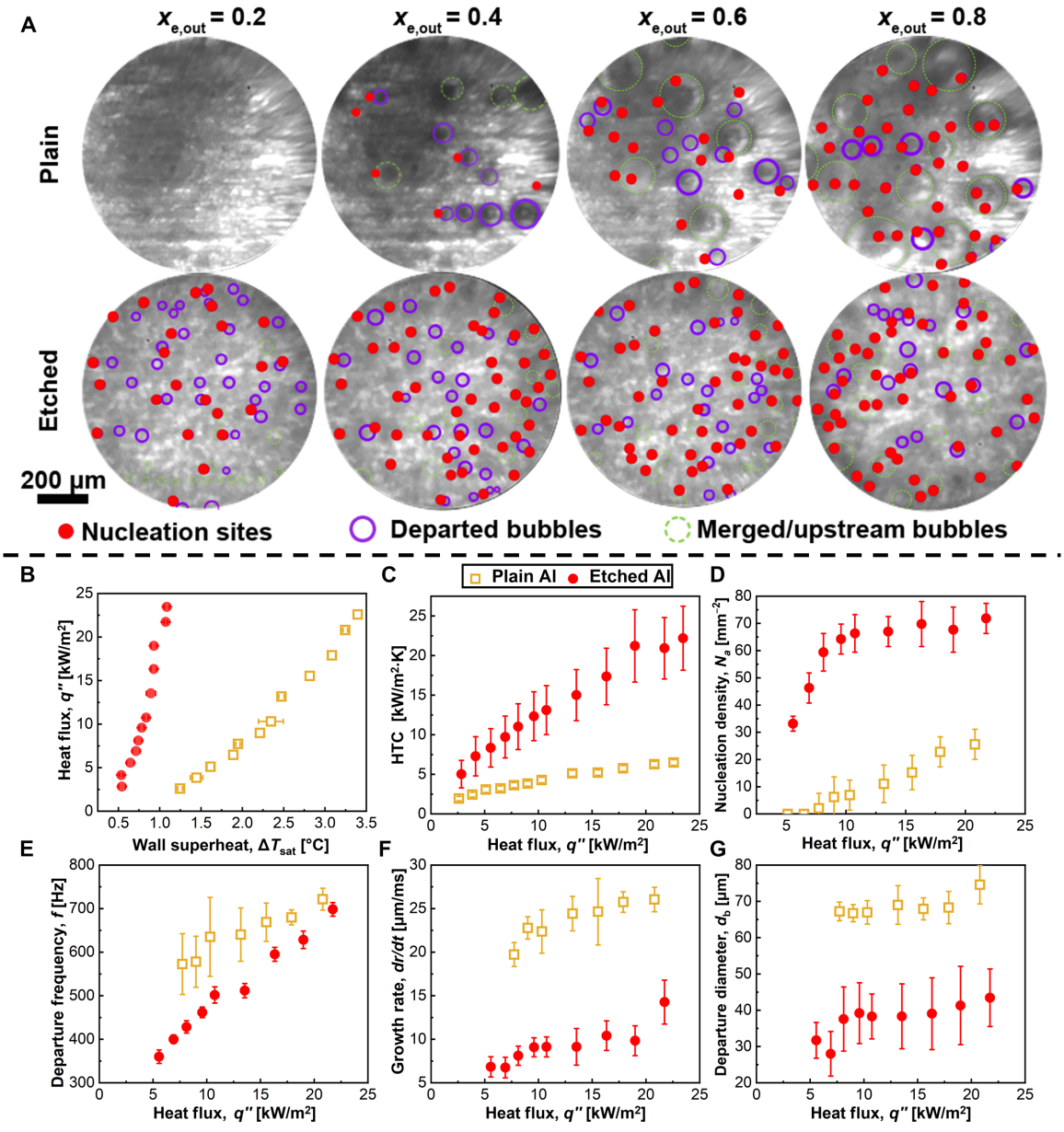

Fig. 3. Analysis of nucleation dynamics for plain and etched Al surfaces. (**A**) Boroscopy photographs at different heat fluxes (q'') for a fixed mass flux $G = 150$ kg/(m^2·s) and a fixed axial location $z = 0.02$ m in the plain (top row; see movie S1) and etched (bottom row; movie S1) Al tubes. For each corresponding heat flux, the tube exit thermodynamic equilibrium quality ($x_{e,out}$) is labeled. Within the photographs, the active nucleation sites are specified with red dots, while the purple circles represent isolated bubbles departed from the corresponding nucleation sites, and green dashed circles represent merged bubbles (not studied here). Full snapshots and time-lapse analysis of the borescope results can be found in text S4 and figs. S3 and S4. (**B**) Wall heat flux (q'') as a function of local wall superheat (ΔT_{sat}), and (**C**) local HTC as a function of wall heat flux (q''), for the plain (yellow hollow squares) and etched (red dots) Al tubes. (**D**) Bubble active nucleation site density (N_a), (**E**) average bubble departure frequency (f), (**F**) average bubble growth rate before departure (dr/dt), and (**G**) average bubble departure diameter (d_b), as a function of wall heat flux (q'') for the plain (yellow hollow squares) and etched (red dots) Al tubes. All experimental data in (B) to (G) are obtained at a length $z = 0.02$ m from the tube inlet (2% axial length) and mass flux $G = 150$ kg/(m^2·s). All average experimental data in (E) to (G) are obtained by arithmetic averaging over the nucleation sites activated at $z = 0.02$ m. Data extraction was hindered by the lack of visible nucleation sites (at sight) at low heat fluxes and by upstream bubble disturbances at high heat fluxes.

wetting nature of the surface structures (table S2). According to the force balance model (*42*), the y-direction forces that determine bubble lift-off, the major bubble departure mechanism observed in this study, are the y-direction surface tension force component ($F_{\sigma y}$), the y-direction unsteady drag force component (F_{udy}, due to the growth of the bubble), the shear lift force (F_{sl}), the hydrodynamic pressure force (F_{hp}), the buoyancy force (F_b), and the contact pressure force (F_{cp}) as shown in Fig. 4A. While the first two forces press the bubbles to the heated surface, the last four forces act to pull the bubble away from the surface. Here, we are not concerned with forces in the z direction which consist of the quasi-steady drag force (F_{qs}), the z-direction surface tension force component ($F_{\sigma z}$), and the z-direction

Downloaded from https://www.science.org at EPF Lausanne on October 12, 2025

unsteady drag force component (F_{udz}). The y component of the surface tension force normal to the boiling surface ($F_{\sigma y}$) acting on a single bubble is (*42*)

$$F_{\sigma y} = -d_c \sigma \frac{\pi}{\theta_a - \theta_r}\left(\cos\theta_r - \cos\theta_a\right) \quad (1)$$

where d_c is the diameter of the contact area, σ is the liquid-vapor surface tension, θ_a is the advancing contact angle, and θ_r is the receding contact angle as measured from the solid-liquid interface to the liquid-vapor interface. On the etched surface, because of the superhydrophilic nature of the surface, both advancing and receding contact angles would go to zero $\theta_a \rightarrow \theta_r \rightarrow 0$ (apparent contact angle, $\theta_{app} \rightarrow 0°$; see table S2). In this limit, $F_{\sigma y} \rightarrow -d_c \sigma \pi \sin(\theta_a)$ (*42*). The near-zero contact angle makes the perimeter of the contact area much smaller when compared to the plain surface, which makes d_c smaller. With a smaller d_c and $\sin(\theta_a) \rightarrow 0$, the surface tension force would be much smaller on the etched surface. This also will result in a smaller inclination angle, ϕ, as $\theta_a \rightarrow \theta_r \rightarrow 0$ as depicted in Fig. 4B. The y component of the unsteady drag force normal to the boiling surface (F_{udy}) acting on an asymmetrically growing single bubble is (*42*)

$$F_{udy} = -\rho_f \pi r^2 \left(r\ddot{r} + \frac{3}{2}\dot{r}^2\right)\cos(\phi) \quad (2)$$

where ρ_f is the liquid density, r is the bubble radius, and $\dot{r}$ and $\ddot{r}$ are the bubble growth rate (dr/dt) and growth acceleration (d^2r/dt^2), respectively. Previous theoretical analysis has shown that the bubble growth rate is dominated by the wall superheat (*43*), which agrees well with our experimental data. The low local wall superheat on the etched surface results in a lower average bubble growth rate (Fig. 3F). This slower average bubble growth (small $\dot{r}$) on the etched surface, alongside an almost constant bubble growth rate ($\ddot{r} \approx 0$) at a fixed heat flux based on experimental observations, leads to a smaller unsteady drag force according to Eq. 2 (with smaller r and $\dot{r}$) (*42*). In total, at the limit of approaching the same bubble size on both an etched and a plain surface, the forces pressing the bubble onto the heated wall (the surface tension force, $F_{\sigma y}$, and the unsteady drag force, F_{udy}) are smaller on the etched surface as compared to a plain surface, while the forces pulling the bubbles away remain the same as shown in Fig. 4 (A and B); F_{sl} and F_b merely depend on the size of the bubble (F_{sl} varies marginally due to a slight difference in liquid velocity at the center of the bubble), meaning that they are the same on both surfaces at this instance, and F_{hp} and F_{cp} that have a dependency on d_c are of much less influence (*42*, *44*, *45*). Hence, the bubble on the etched surface will depart as $d \rightarrow d_b$, while the bubble on the plain surface would keep growing until it reaches its larger bubble departure diameter at mechanical equilibrium. As a result, the average bubble departure diameter (d_b) on the etched Al surface is smaller when compared to the plain Al surface. We also carried out a more quantitative analysis to better confirm these hypotheses in which we calculated the forces acting on vapor bubbles of the same size on the etched and plain Al surfaces. We take the experimental values of the bubble departure diameter of the etched Al and base our calculation of pain Al on the very same sizes. On the basis of our calculations (please see text S5 and fig. S6) of the unsteady drag force, at the very instance described in Fig. 4 (same bubble sizes), the absolute value of unsteady drag force, $|F_{udy}|$, on the plain surface varies between ~1 and 2 nN (for varying heat flux), while at the same sizes on the etched surface, it varies between ~0.1 and 0.5 nN (for varying heat flux) for the case of $G = 150$ kg/(m^2·s). Further

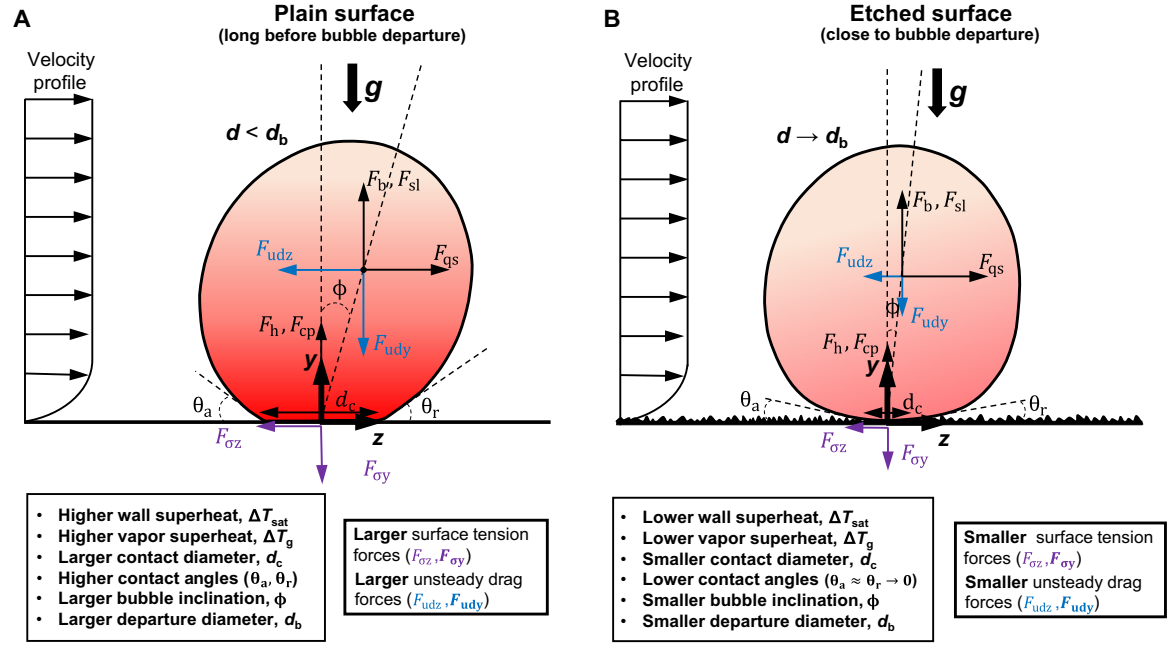

Fig. 4. Comparison of forces acting on a bubble on plain and etched surfaces. Schematic comparison of forces acting on a single bubble growing at any given nucleation site up to a fixed bubble size during saturated flow boiling on a heated (**A**) plain and (**B**) etched surface. Mainly, on the etched surface, the unsteady drag forces (F_{udz}, F_{udy}) are smaller due to lower wall superheat, and surface tension forces ($F_{\sigma z}$, $F_{\sigma y}$) are smaller due to a smaller contact area and contact angle. The upward forces remain approximately the same on both surfaces resulting in an earlier bubble departure on the etched surface. For a comprehensive quantitative analysis, please refer to text S5 and fig. S6.

Downloaded from https://www.science.org at EPF Lausanne on October 12, 2025

calculation of other forces to get the net y-directional force (please see text S5 and fig. S6) also shows that, in general, at the very instance described in Fig. 4, the net force is positive (closer to zero) on the etched surface (signifying bubble departure as $d \rightarrow d_b$) and far negative on the plain surface (signifying the bubble is far away from departure as $d < d_b$).

The experimentally measured average bubble growth rate for each surface is much higher than what the bubble growth model suggests (*43*), which makes unsteady drag force no longer negligible when compared to other forces acting on the bubble, in agreement with the observations of Klausner *et al.* (*42*). The high experimentally measured average bubble growth rate indicates that the unsteady drag force is a dominant factor in determining bubble behavior. From Fig. 3B, we see that the local wall superheat (ΔT_{sat}) increases with the heat flux (q''), which means that the unsteady drag force on the bubbles also increases with heat flux due to the corresponding increase in average bubble growth rate. As a result, with a larger unsteady drag force further pressing the bubble on the surface, the average bubble departure diameter (d_b) is larger at higher heat fluxes as shown in Fig. 3G. We further confirmed this through quantitative calculations (please see text S5). It is evident from fig. S5 that the unsteady drag force increases with heat flux for both plain and etched surfaces (with the increase in wall superheat, ΔT_{sat}) resulting in an increasing trend in bubble departure diameters with heat flux for all mass fluxes (figs. S4 and S5). It is suggested that as the bubble approaches lift-off ($d \rightarrow d_b$), $d_c \rightarrow 0$; hence, $F_{\sigma y}$, F_{hp}, and $F_{cp} \rightarrow 0$ (*44*). This would leave the unsteady drag force caused by the rapid growth of the bubble to be the dominant downward force in our experiments as the bubble approaches lift-off ($d \rightarrow d_b$). The dominant upward forces are hence the shear-lift force (F_{sl}) and the buoyancy force (F_b) calculated (*44*) as the following

$$F_{sl} = 1.94\rho_f \Delta U^2 \pi r^2 \left(\left| \frac{dU}{dy} \right| \frac{r}{\Delta U} \right)^{1/2} \left[\frac{1}{Re_r^2} + 0.014 \left(\left| \frac{dU}{dy} \right| \frac{r}{\Delta U} \right)^2 \right]^{1/4} \quad (3)$$

$$F_b = \frac{4}{3}\pi r^3 (\rho_f - \rho_g) g \quad (4)$$

where ΔU is the difference between the fluid velocity at the center of the bubble and velocity of the bubble, y is the distance away from the surface to the centerline, Re_r is the bubble Reynolds number ($Re_r = \rho_f \Delta U d/\mu_f$, where μ_f is the liquid viscosity), and ρ_f and ρ_g are the fluid and vapor density, respectively. With an increase in unsteady drag force and a corresponding increase in bubble diameter with heat flux for different mass fluxes (fig. S5C), both the forces pulling the bubble away from the surface also increase until they achieve mechanical equilibrium at departure (as $d \rightarrow d_b$) (fig. S5, A and B). From Eq. 3, it is evident that mass flux (G) tends to dominate the shear lift force (F_{sl}) due to its dependency on the velocity gradient ($|dU/dy|$) near the wall. An increase in mass flux increases the bubble shear lift force (fig. S5A), which leads to a larger force pulling the bubble away from the heated surface. Hence, a higher mass flux results in a slightly smaller bubble departure diameter (*42*, *44*), as observed in our results for different mass fluxes [see figs. S4 (D to F) and S5A]. This slight decrease in bubble departure diameter with mass flux also results in a smaller buoyancy force as evident in fig. S5B.

The lower local wall superheat on the etched surface not only results in a smaller average bubble growth rate but also leads to a lower average bubble departure frequency (Fig. 3E). The bubble departure frequency for a single bubble is essentially the inverse of the bubble residence time, which is the sum of the growth time and wait time of the bubble on a heated surface. The growth time can be approximately calculated by dividing the bubble departure radius by the growth rate. As both values are smaller for the etched surface, direct judgment based on the ratio is not feasible. However, the experimental values (direct measurement of average growth time) show that the average growth time on the etched surface is always longer. For example, at mass flux $G = 150$ kg/(m^2·s) and heat flux q'' ≈11 kW/m^2 (the case of movie S1), the typical bubble average growth time on the etched Al surface is ≈2.1 ms, while the average growth time on the plain Al surface is only ≈1.5 ms. Regarding the wait time, because refrigerants have lower surface tension and latent heat of vaporization compared to other room temperature working fluids such as water, both plain and etched Al surfaces typically experience low wall superheats. This happens because vapor formation and bubble departure occur more easily for refrigerants. For instance, for the highest heat flux and highest mass flux, the local wall superheat near the entrance ($z = 0.02$ m) is $\Delta T_{sat} \approx 1$°C for the etched Al surface and $\Delta T_{sat} \approx 4$°C for the plain Al surface (see text S7 and fig. S7). This means that the average wait time, which is the time required to achieve the required wall superheat for nucleation after the departure of the previous bubble, is negligible [wait time will also further reduce with heat flux as literature suggests (*46*, *47*)] when compared to the average growth time (one order of magnitude smaller based on experimental values). As a result, the average bubble departure frequency on the plain surface is higher than that on the etched surface as shown in Fig. 3E with smaller growth times. As the heat flux increases, the average bubble growth rate also increases (Fig. 3F), leading to a decrease in the average growth time and an increase in the average bubble departure frequency (Fig. 3E) (*43*).

Boroscopy enabled bubble dynamics analysis: Copper

To further test our hypotheses and delve deeper into the effect of surface morphology on heat transfer characteristics, we next carried out additional boroscopy imaging experiments at the identical entrance location ($z = 0.02$ m corresponding to 2% axial length) and mass flux on plain Cu and etched Cu surfaces. Figure 5A shows that, although the etched Cu surface results in a slightly higher number of nucleation sites, the differences between the two surfaces are much less pronounced when compared to the observations from Al surfaces. This consequently results in a lower reduction in local wall superheat as evident from Fig. 5B, which leads to a relatively lower local HTC enhancement of around 25% on average (for different heat fluxes) and a maximum local HTC enhancement of 38% (Fig. 5C), when compared to etched Al surface. The analyzed boroscopy imaging results are presented in Fig. 5 (D to G). As the local wall superheat (see Fig. 5B, text S7, and fig. S8) does not change appreciably, the growth rate (Fig. 5F) and consequently the unsteady drag force and departure frequency (Fig. 5E) do not change appreciably. Furthermore, the contact angle (see table S2 and text S3) does not show a notable change for the etched Cu sample as compared to the plain Cu sample; thus, the surface tension force will not change substantially. As a result of having both forces pressing the bubble on the surface almost remaining the same and having the forces pulling the

Downloaded from https://www.science.org at EPF Lausanne on October 12, 2025

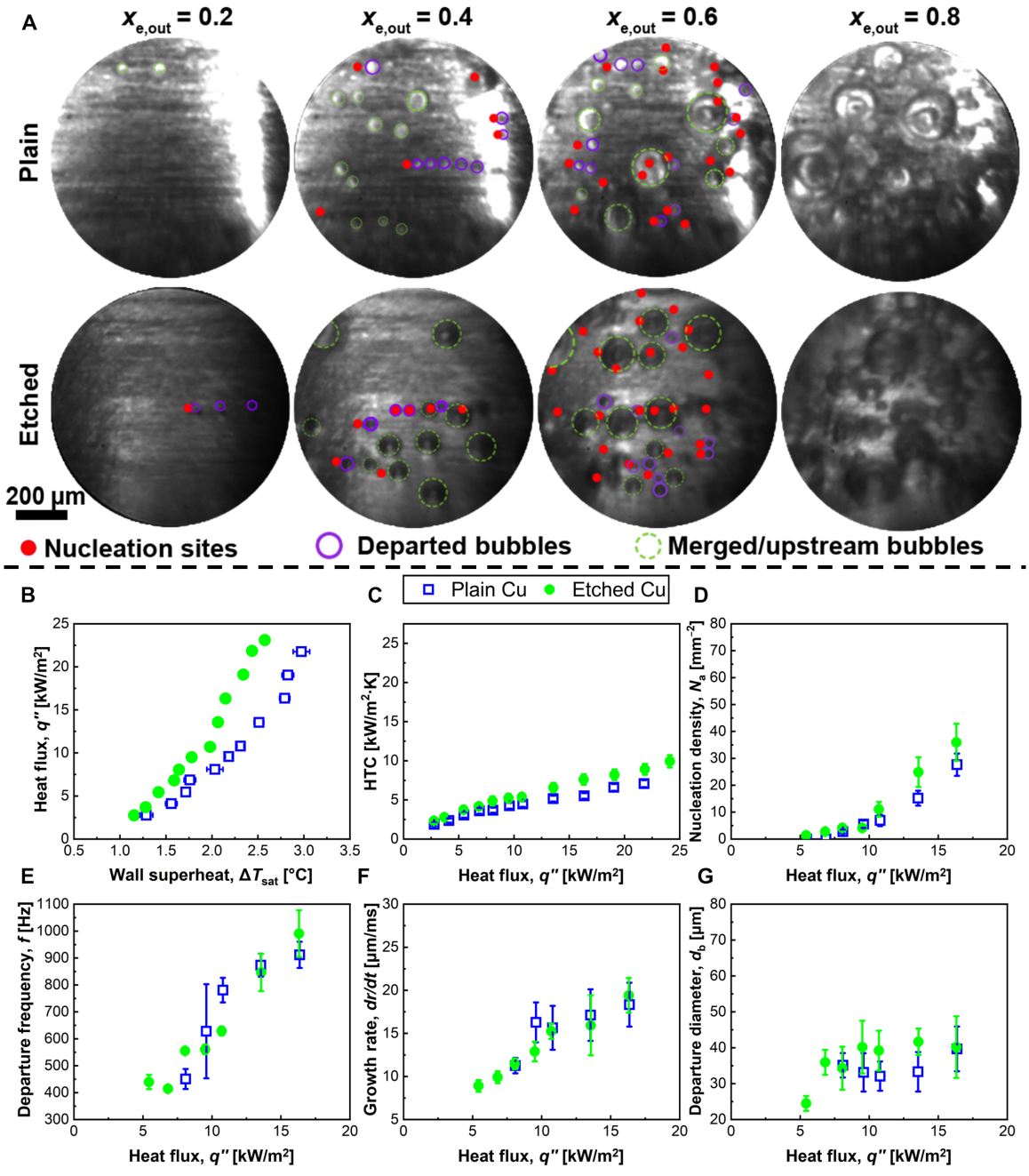

Fig. 5. Analysis of nucleation dynamics for plain and etched Cu surfaces. (**A**) Boroscopy photographs at different heat fluxes (q'') for mass flux $G = 150$ kg/(m^2·s) and a fixed axial location $z = 0.02$ m in the plain (top row; movie S2) and etched (bottom row; see movie S2) Cu tubes. For each corresponding heat flux, the tube exit thermodynamic equilibrium quality ($x_{e,out}$) is labeled. Within the photographs, the active nucleation sites are specified with red dots, while the purple circles represent isolated bubbles departed from the corresponding nucleation sites, and green dashed circles represent merged bubbles (not studied here). (**B**) Wall heat flux (q'') as a function of local wall superheat (ΔT_{sat}) and (**C**) local HTC as a function of wall heat flux (q'') for the plain (blue hollow squares) and etched (green dots) Cu tubes. (**D**) Bubble active nucleation site density (N_a), (**E**) average bubble departure frequency (f), (**F**) average bubble growth rate before departure (dr/dt), and (**G**) average bubble departure diameter (d_b), as a function of wall heat flux (q'') for the plain (blue hollow squares) and etched (green dots) Cu tubes. All experimental data in (B) to (G) are obtained at a length $z = 0.02$ m from the tube inlet (2% axial length) and mass flux $G = 150$ kg/(m^2·s). All average experimental data in (E) to (G) are obtained by arithmetic averaging over the nucleation sites activated at $z = 0.02$ m. For lower heat flux conditions, data extraction was impeded because of the absence of visible nucleation sites in the observation window, and for high heat flux situations, it became unfeasible due to disturbances caused by upstream bubbles.

Downloaded from https://www.science.org at EPF Lausanne on October 12, 2025

bubble away almost remaining the same (same as for Al), the average bubble departure diameter does not undergo a substantial change after Cu etching (Fig. 5G).

Surface structure sizes: Key to the boiling heat transfer enhancement

In general, we observe a strong correlation between HTC enhancement on structured surfaces and their corresponding bubble dynamics. Our boroscopy method reveals that certain surfaces have the potential to augment HTC by amplifying the active bubble nucleation density. The distinctions in the level of HTC enhancement between etched Al (versus plain Al) and etched Cu (versus plain Cu) surfaces can be attributed to the variations in their respective bubble dynamics caused by distinct levels of etching achieved on the surface for the respective metals. However, the intriguing question persists as to why these contrasting bubble dynamics emerge on seemingly similar rough surfaces. The active nucleation cavity size range for our experiments was calculated to be dominantly at the micron-scale (see text S8 and fig. S9) for our specific surfaces, operating conditions, and working fluid. In short, the desired cavity size range for active nucleation is deduced when the available liquid superheat within the laminar sublayer at a distance r away from the heated surface [$\Delta T_f = T_f - T_{sat} = \Delta T_{sat} - (q''/k_f)r$; where k_f is the fluid thermal conductivity and T_f is the liquid temperature] meets and exceeds the required vapor superheat ($\Delta T_g = T_g - T_{sat} = 2\sigma T_{sat}\nu_{fg}/h_{fg}r$; where ν_{fg} is the difference in specific volumes of vapor and liquid) for sustaining an embryo bubble of radius r as depicted in Fig. 6A. When $r \rightarrow 0$ [for bubble radii from very small cavities, as cavity mouth radius and bubble radius originating from that cavity are related (*48*)], the required vapor superheat goes to infinity, $\Delta T_g \rightarrow \infty$. However, as r increases, a point is reached where the available liquid superheat, ΔT_f, matches the required vapor superheat (the first intersection of required vapor superheat and available liquid superheat curves in Fig. 6A), identifying the smallest cavity that can be activated. With a further increase in r (originating from larger cavities), the required vapor superheat goes down. However, moving further away from the wall (with the increase in r), the available liquid superheat is reduced further. Eventually, there is a second

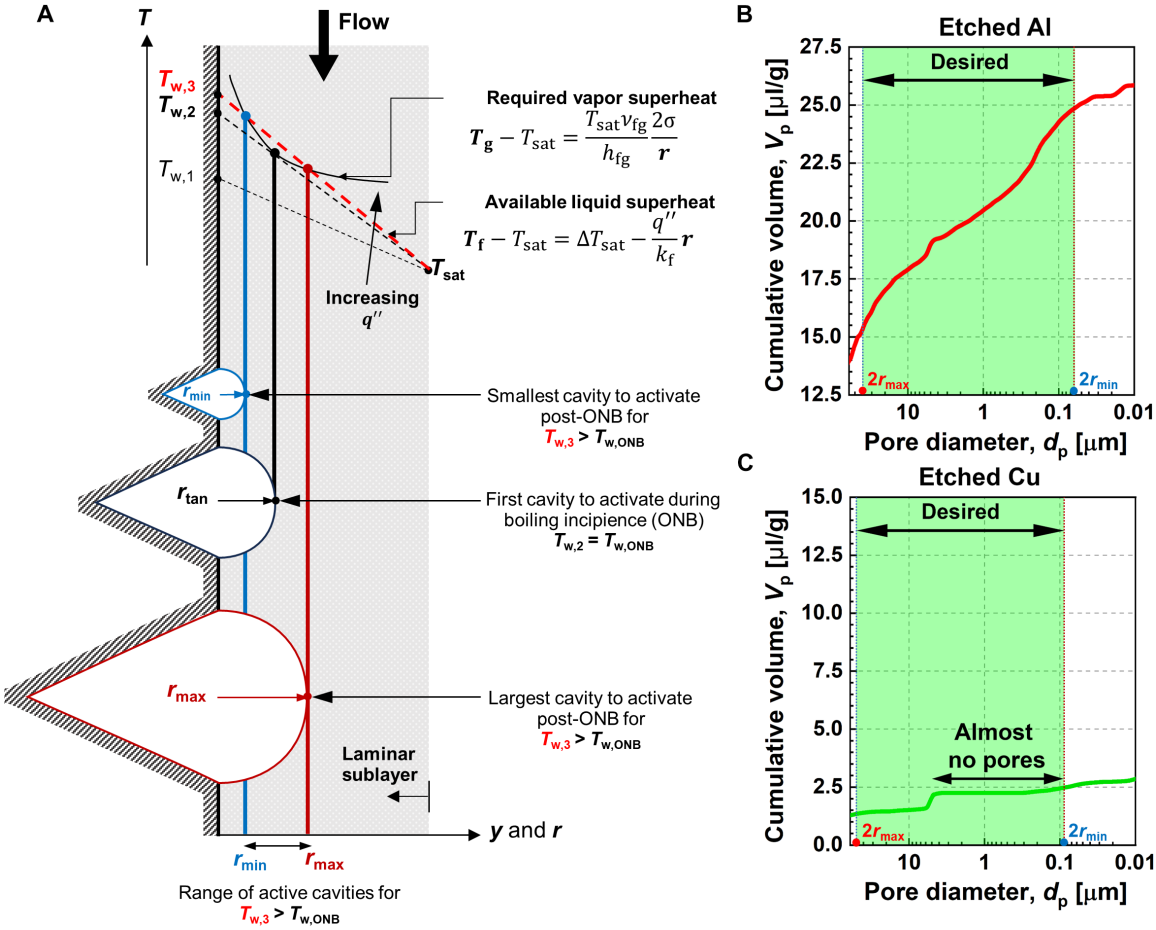

Fig. 6. Activation criteria for nucleation cavities and porosity analysis of etched Al and Cu surfaces. (**A**) Schematic representation for the criterion to determine cavities activated for nucleation during saturated flow boiling. $T_{w,1}$, $T_{w,2}$, and $T_{w,3}$ are the wall temperatures below, at, and above the onset of nucleate boiling ($T_{w,ONB}$), respectively. Mercury porosimetry results for (**B**) etched Al and (**C**) etched Cu surfaces. While Cu structures mostly fail to provide cavities in the desired range, the Al structures have pores ranging in size from nanoscale to microscale. Note that the cumulative penetration volume for etched Al is almost 10 times that of the etched Cu as it is much more porous immediately beneath the surface. This unique characteristic cannot be quantified using classical SEM, FIB-assisted cross-sectional SEM, or confocal microscopy analyses. Light-shaded green regions represent the desired cavity size distribution for flow boiling heat transfer enhancement via nucleate boiling for $G = 150$ kg/(m^2·s) for a wall superheat of $\Delta T_s = 4$°C (see text S7 and fig. S7).

Downloaded from https://www.science.org at EPF Lausanne on October 12, 2025

point where the available liquid superheat and required vapor superheat match, determining the largest cavity that can be activated (second intersection of required vapor superheat and available liquid superheat curves in Fig. 6A). This gives the range of cavity sizes for active nucleation sites at a particular wall superheat (please see text S8 and fig. S9) (*49*). This analysis also reveals that the required vapor superheat (ΔT_g) for nucleating an embryo bubble within a larger cavity (large r) is smaller as it scales inversely with r ($\Delta T_g \sim 1/r$). Thus, surfaces with large and active cavities (that can successfully trap a vapor embryo), specifically in large numbers, can offer much better heat transfer performance.

It appears from SEM and FIB-aided cross-sectional SEM images of Fig. 1 that both etched Al and etched Cu have approximately identical pore/cavity sizes at the surface [see Fig. 1 (B and D)]. However, despite the apparent similarity of the surfaces, they exhibit extremely different heat transfer behavior. To better quantify the apparent disparity between the etched Al and etched Cu surfaces, we needed a better method for characterizing the surface morphologies at the microscale. Conventional surface characterization methods such as SEM, FIB-SEM, atomic force microscopy, and confocal microscopy can only render qualitative comparisons (see Fig. 1) at the surface of the sample. Pores may extend beneath the surface, and hence a technique that can probe these pores and their distribution is needed for a rigorous quantitative comparison. For this purpose, we used mercury porosimetry (see text S1). Figure 6 (B and C) presents the mercury porosimetry results. First, it is observed from Fig. 6 (B and C) that the penetration volume for the etched Al surface surpasses that of etched Cu by one order of magnitude, signifying a substantially greater level of roughness and thus greater porosity on the etched Al surface. Specifically, Fig. 6 (B and C) depicts that the etched Al surface uniformly provides pores within a broad range of sizes in the desired range for active nucleate boiling (with a high number of large and active cavities, see text S8 and fig. S9). In contrast, the etched Cu surface is mostly incapable of providing pores in the desired range. Thus, it is deduced that the etched Al surface renders a greater number of pores/cavities in the desired range, specifically larger cavities in the micron-scale, and can exhibit more pronounced HTC enhancements. The required vapor superheat scales inversely with r ($\Delta T_g \sim 1/r$), and on the etched Al surface with many large active cavities, the wall superheat did not exceed ~1°C in our experiments, contributing to heat transfer enhancement (HTC $\propto 1/\Delta T_{sat}$). It is important to note that similar macroscale heat transfer performance trends were observed with these structures using other working fluids (*37*, *50*). However, as these efforts have been only limited to analysis of macroscopic system-level responses such as surface temperature and pressure drop, they were unable to explain the intricate relations between bubble dynamics, surface characteristics, and heat transfer performance. Mechanisms that are addressed with our in situ visualization offer deeper insights into the effects of cavity size variations on bubble dynamics and heat transfer performance.

The differences in the pore size distribution of the etched Al and etched Cu surfaces can be attributed to their different etching mechanisms. Aluminum is etched using HCl, a potent acid that reacts with Al to produce aluminum chloride ($AlCl_3$) and hydrogen gas (H_2). The reaction between the two is exothermic, leading to an increased temperature of the solution, further amplifying the etch rate. As a result, a rough surface is produced with ideal cavity sizes for boiling due to the high etch rate and the pronounced evolution of H_2 bubbles on the surface during the reaction (*51*). In contrast, Cu cannot be etched using HCl, and it is typically etched using ferric chloride ($FeCl_3$). Copper is less reactive with $FeCl_3$, which results in a much slower etch rate. Furthermore, $FeCl_3$ also tends to form a passive layer on the surface of Cu, which further slows down the etch rate and limits the formation of micro and nanoscale features beneath the surface (*52*). It is worth noting that, later, we developed other etching chemistries for Cu that resulted in larger cavity sizes such as the ones observed on etched Al that demonstrated high HTCs that further supported our discussions on cavity sizes and its material independence (please see text S9 and fig. S10).

Further effects of structures on actual vapor quality and flow regime

The results of the boroscopy experiments conducted at an axial length of 30% of the heated tube ($z = 0.3$ m) are shown in Fig. 7 (A and B) and fig. S11 (see text S10). The results show that the etched Al surface results in a much higher vapor generation, and the flow becomes so bubbly that the phenomena occurring beneath coalesced bubbles could not be discerned (see movie S3). The remarkable increase in vapor content in the bubbly flow is again indicative of a substantial increase in bubble nucleation density. As expected, etched and plain Cu surfaces appear to be similar to each other in terms of bubble dynamic characteristics (see movie S3), in agreement with the measured HTC data showing lower enhancement levels for etched Cu (versus plain Cu) when compared to etched Al (versus plain Al). An important observation derived from these visual representations is that with the etched surfaces, specifically with the etched Al, the actual quality (x), which is always lower than the calculated thermodynamic equilibrium quality (x_e) during saturated flow boiling on plain surfaces (*53*), exhibits a progressive convergence toward it ($x \rightarrow x_e$), given the existence of much more active nucleation sites on etched surfaces which reduces the superheating of the vapor bubbles departing from the surface and thus reducing the thermal nonequilibrium.

To study the effects of surface structuring on flow regimes and to see if additional effects other than nucleation density are important, we next analyzed the boroscopy imaging results obtained near the tube exit ($z = 0.95$ m, 95% of axial length), and the results are presented in Fig. 7 (C and D). It is well understood that pure annular flow is achieved when a thin film of liquid flows along the inner surface of the tube, whereas the vapor phase occupies the central core of the tube (with an annulus shape) while no bubbles are seen nucleating or sliding in the thin liquid film (Fig. 8, A and B). Bearing that in mind, the point at which the transition to pure annular flow (where no bubbles are observed) occurs was investigated. Figure 7 (C and D) shows that this transition is generally delayed for tubes with structured surfaces. This is primarily because of the lowering of the wall superheat required for bubble nucleation on structured surfaces as observed in Fig. 3B for etched Al and, to a lesser extent, in Fig. 5B for etched Cu. This transition that denotes the complete suppression of nucleate boiling is thus delayed for structured surfaces as depicted in Fig. 7 (C and D). This delay in boiling suppression serves as an additional mechanism governing the observed enhancements in HTC on structured surfaces due to prolonged nucleation occurring on relatively more active nucleation sites leading to more vapor bubbles with lower superheating being easily generated at lower wall superheats. Conversely, when it comes to pure annular flow where complete suppression of nucleate boiling occurs, these structured

Downloaded from https://www.science.org at EPF Lausanne on October 12, 2025

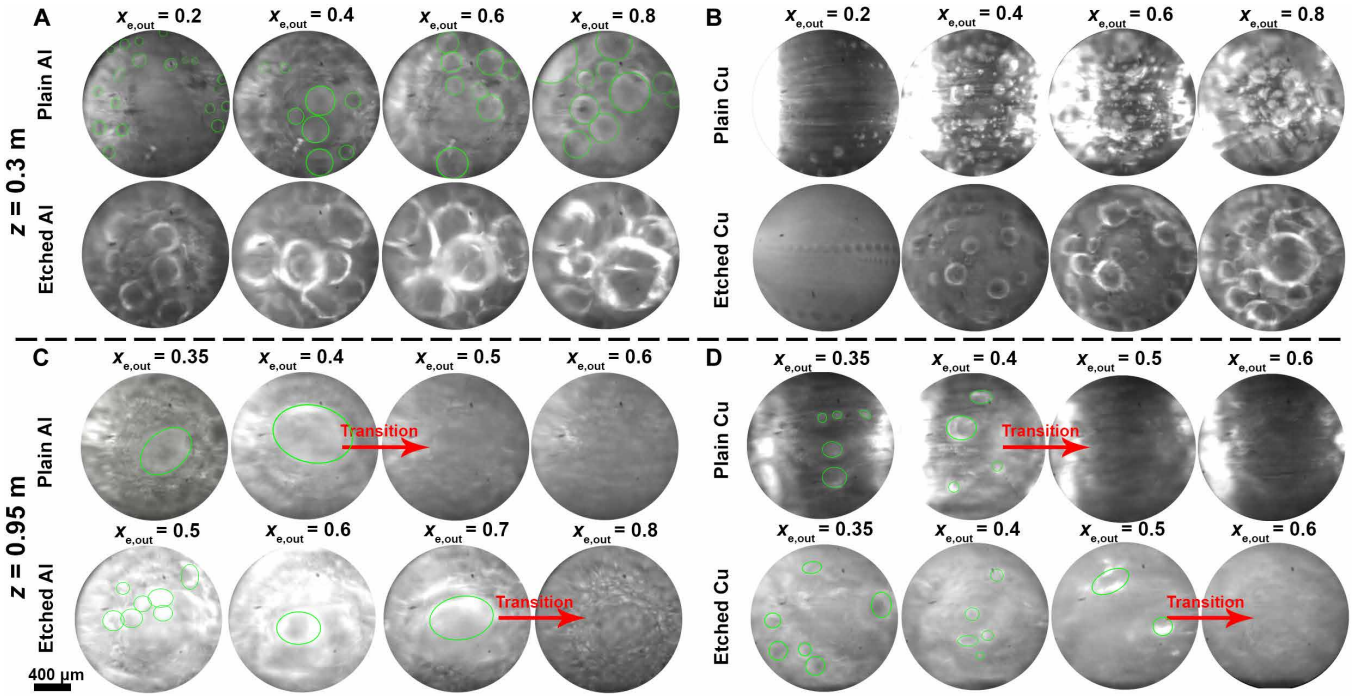

Fig. 7. Comparative boroscopy analysis of actual flow quality and flow regimes in Al and Cu tubes at different axial lengths. Boroscopy photographs of the tubes for (**A**) plain Al and etched Al and (**B**) plain Cu and etched Cu surfaces at $G = 150$ kg/(m^2·s), where the borescope is inserted at the 30% axial length ($z = 0.3$ m). It is observed that the actual quality (x) on the etched surfaces is higher and thus closer to the theoretical thermodynamic equilibrium quality (x_e); more specifically, the etched Al surface seems to be the closest to having $x \approx x_e$. Boroscopy photographs of the tubes for (**C**) plain Al and etched Al and (**D**) plain Cu and etched Cu surfaces at $G = 150$ kg/(m^2·s), where the borescope is inserted near the exit at 95% axial length ($z = 0.95$ m). It is evident that the transition to pure annular flow where no bubbles are observed is generally delayed on the etched surfaces which helps the persistence of nucleate boiling (where the main enhancement mechanism exists). For more clarity, some bubbles are marked with green shapes. For additional borescope photographs at 30% length and near the exit of the tube, please refer to text S8 and figs. S8 and S9.

surfaces do not actively participate in heat transfer enhancement. Because of the higher void fraction (α, defined as the ratio of flow area occupied by vapor to the total flow area) in tubes using etched surface, the already thin liquid film undergoes further thinning due to macrolayer evaporation, which, in turn, gradually reduces the thermal resistance in the liquid film, thereby only slightly increasing the HTC in the annular flow (*35*).

Comparing our data shown in Fig. 7 (C and D) as well as in fig. S12 reveals that the transition to pure annular flow occurs at lower heat fluxes as the mass flux is increased, which is expected in all general flow regime maps (*54*). The reason for this behavior is that increasing the mass flux reduces the wall superheat by enhancing convection near the surface. Thus, the transition point to pure annular flow where the wall superheat is lower than the minimum required wall superheat for nucleate boiling ($\Delta T_{w,ONB}$) happens earlier (i.e., for a lower wall heat flux). It is evident that the magnitude of this delay is higher for Al (etched versus plain) when compared to Cu (etched versus plain) surface. This is in accordance with the HTC data as etching Al prolonged nucleation by creating relatively higher active nucleation sites even at lower wall superheats when compared to etching Cu. Our results emphasize the need for further experimentation to raise awareness about the importance of avoiding the use of conventional two-phase flow boiling correlations and flow regime maps that are designed for plain surfaces when predicting performance on structured surfaces.

Dryout dynamics

As surface structures are known to increase capillarity within the thin annular liquid film, we conducted a characterization of the dryout dynamics on the surfaces. Dryout at CHF was investigated by increasing the heat flux to the point that the thin-liquid film on the surface partially dried out near the exit and the corresponding local wall temperature increased rapidly and exhibited periodic fluctuations, resulting in a sudden decrease in the local HTC (*55*). The partial dryout (henceforth referred to as simply dryout) for both the plain and etched Al tubes at $G = 150$ kg/(m^2·s) occurred at approximate exit thermodynamic equilibrium qualities of $x_{e,out} \approx 0.88 \pm 0.01$ and $x_{e,out} \approx 0.87 \pm 0.01$, respectively. Dryout for the plain Cu surface occurred at $x_{e,out} \approx 0.80 \pm 0.01$, while for the etched Cu tube, it occurred at $x_{e,out} \approx 0.88 \pm 0.01$. In general, the potential for delaying dryout to higher $x_{e,out}$ is very limited in our experiments since the refrigerant (R515B) liquid-vapor surface tension and latent heat of vaporization are relatively low ($\sigma = 8.76$ mN/m and $h_{fg} = 162.43$ kJ/kg at 25°C). This in conjunction with effective surface wetting by the refrigerant causes the dryout within the thin annular liquid film to occur at relatively higher exit qualities. In contrast, multiple works have reported achieving a notable delay in dryout exit thermodynamic equilibrium qualities using water (*8*, *9*) particularly in microchannels with structured surfaces by delaying $x_{e,out}$ from 0.1 to 0.3. With relatively higher surface tension and latent heat of vaporization for water ($\sigma = 71.8$ mN/m and $h_{fg} = 2441.7$ kJ/kg at 25°C),

Downloaded from https://www.science.org at EPF Lausanne on October 12, 2025

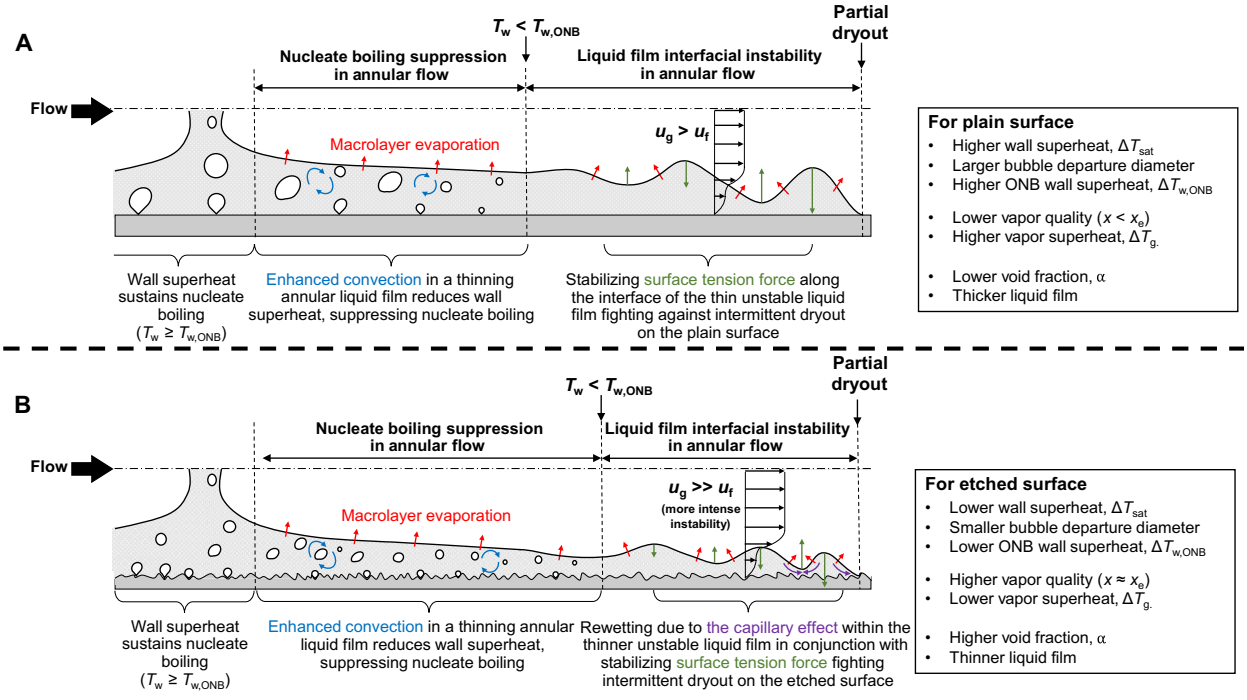

Fig. 8. Interfacial dynamics in the annular flow regime on plain and etched surfaces. Schematic representation of stabilizing and destabilizing interfacial physics occurring within the annular flow regime leading to partial dryout during saturated flow boiling in a tube having (**A**) plain surface and (**B**) etched surface. The higher rate of nucleation on the etched surface results in a higher void fraction (α) and consequently a thinner liquid film and a more pronounced difference between the velocity of the vapor and liquid. This results in a more intense destabilization of the interface held together by the surface tension and favorable capillary effect introduced by the structures (opposing mechanisms).

structured surfaces seem to exhibit a higher potential to improve surface wettability and thus delay dryout very effectively for water as compared to a refrigerant.

The absence of any observed dryout delay with etching Al compared to etching Cu seemed counterintuitive as etched Al is much more porous. Moreover, we found it unusual that dryout on the plain Al surface occurred at a higher exit thermodynamic equilibrium quality ($x_{e,out}$) when compared to the plain Cu surface. To investigate these differences further, we conducted confocal microscopy on the tube samples through axial cross sectioning of the real tubes used in the flow boiling experiments (see text S11 and figs. S13 and S14). Our analysis revealed that the plain Al surface exhibited a high degree of roughness [root mean square (RMS) roughness: 1.31 ± 0.27 μm], whereas the plain Cu surface was much smoother (RMS roughness: 0.23 ± 0.08 μm). The greater wetting capability of the plain Al because of higher surface roughness facilitated its superior performance over plain Cu with regard to tube exit thermodynamic equilibrium quality at dryout. However, there appeared to be an upper limit on the maximum delay in $x_{e,out}$ at dryout, which we determined to be $x_{e,out} \approx 0.88$. Notably, despite its much greater surface roughness (etched Al RMS roughness: 9.80 ± 0.43 μm), the etched Al surface provided almost no delay in dryout, indicating that the maximum enhancement was already achieved. Conversely, as plain Cu is inherently very smooth, a slight increase in surface roughness (etched Cu RMS roughness: 0.59 ± 0.14 μm) proved effective in delaying dryout to slightly higher $x_{e,out}$. Full visualizations of the dryout phenomenon on these surfaces can be observed in text S6 and movie S5.

To investigate the underlying mechanisms behind minimal or no delay in dryout with etched/structured surfaces, a detailed side-view visualization is crucial to measure the thickness of the thin liquid film and the amplitude and wavelength of the liquid-vapor interface particularly near partial dryout location. However, the top-view boroscopy falls short in providing this level of insight (although the interfacial instability-induced wavy interfaces are visible near dryout location in movie S5). In our previous investigations, we have proved that these structures make the liquid film thinner (achieved via higher void fraction by virtue of higher actual quality at lower wall superheats on structured surfaces as shown here too) (*18*, *34*, *35*). Given that, one possible explanation for not seeing a substantial delay in dryout (judging based on exit thermodynamic equilibrium quality) could be the following dual effects caused by the surface structures. Although these structures are promised to enhance capillary pressure, they also increase the actual quality with more nucleation, with actual quality asymptotically reaching the thermodynamic equilibrium quality ($x \rightarrow x_e$). This, in turn, leads to further thinning of the liquid film (favorable for HTC via thin-film conduction) by increasing the void fraction with vapor quality which results in a higher slip ratio ($S = u_g/u_f$, u_g = vapor velocity, u_f = liquid velocity). This effect is much more pronounced at higher actual qualities (see text S12 and fig. S15). Specifically, when $x > 0.8$, the difference between u_g and u_f increases drastically (fig. S15), which correspondingly also increases the interfacial instabilities (*56*). These two competing mechanisms (enhancing capillarity and aggravating interfacial instabilities) in turn result in almost no dryout delay (Fig. 8, A and B). However, it is important to note that our metric for comparing

Downloaded from https://www.science.org at EPF Lausanne on October 12, 2025

dryout performance for the plain and etched surfaces is the thermodynamic equilibrium quality calculated from the energy balance. As it was shown that on the etched surfaces, the actual quality is higher, there might exist some enhancement in dryout if we compare the surfaces based on actual quality.

It is important to note that the observed dryout dynamics and lack of an appreciable effect on delaying the dryout process using our generated etched structures are also attributed to the relatively small length scale of our structures. In particular, the thickness of our surface features is quite small compared to more classical surface structuring dryout enhancing mechanisms such as wicks or pillars (*8*, *57*). Hence, the capillary pressure generated within our surfaces is limited by their feature height and operates in a regime where limited dryout delay is observed. However, most past configurations have limitations in terms of scalability or manufacturing, and their applicability to practical real-world scenarios is limited. In addition, given the marginal potential for improvement with refrigerants (CHF at $x_{e,out} \approx 0.8$ to 0.87), opting to compromise scalability in pursuit of a minor CHF enhancement may be unwise from a practical standpoint.

Future perspectives

The present study investigated the role of surface structures on heat transfer performance using in situ and in-liquid boroscopy. The unprecedented direct visualizations presented here substantially enhance our understanding of flow boiling heat transfer phenomena and serve as a valuable benchmark for previous theoretical models and simulation results (*58*). Most two-phase flow simulation tools suffer from a lack of physically relevant data for validation. Numerical submodels for the entrance fluid velocity profile, surface roughness, and its correlation to bubble nucleation density, departure size, and departure frequency are all key experimental parameters that must be known to establish proper boundary conditions within the simulation, as well as to verify the simulation results (*59*). Our boroscopy platform not only provides essential nucleation parameters but also enables the simultaneous direct observation of relevant flow physics within the liquid flow continuum.

Moreover, the findings suggest several avenues for further research and exploration to deepen our understanding of the underlying mechanisms and extend the applicability of structured surfaces to a variety of other scenarios. One aspect that deserves future attention is the study of thin-film flow boiling. Insertion of the borescope from the side can potentially enable accurate in situ measurements of the thin liquid film profile alongside other valuable parameters such as wavelength and amplitude of the moving liquid-vapor interface near dryout, a key metric to understanding capillary waves and boiling crisis instability. In addition, we used a low GWP and low ODP refrigerant (R515B) in this study. Exploration of other low GWP and ODP alternatives such as zeotropic and azeotropic blends can provide a broader understanding of surface performance under varied thermal and environmental conditions, essential for sustainable heat transfer solutions and design guidelines. Several low GWP alternatives that have a high potential for aiding decarbonization efforts in building energy systems are classified as zeotropic blends. These blends consist of a mixture of refrigerants. The properties are a combination of the individual component properties, and the vapor composition is different from the liquid, promoting fractionation and temperature glide (*60*). The physical mechanisms governing two-phase flows and heat transfer of zeotropic blends are more difficult to discern when compared to their azeotropic alternatives (*61*), motivating our in-liquid boroscopy method as a promising technique to help understand the flows.

Furthermore, as an excellent correlation was observed between bubble dynamics and heat transfer characteristics, incorporating artificial intelligence (AI) and machine learning techniques to analyze experimental data could facilitate further pattern recognition, heat transfer correlation development, and extrapolation of results beyond the experimental range (*62*). This data-driven approach would aid in generating predictive models for surface optimization and performance estimation under different scenarios (*63*). To attain meaningful extrapolation-based AI, the presented results should first be used to verify and develop high-fidelity numerical models of two-phase flows (*64*). These models can then be used to generate the data needed to train models capable of meaningful physics-based extrapolation to accurately predict performance in test regimes that are not capable of being reached using experiments.

The boroscopy technique showcased here for flow boiling and previously for pool boiling (*32*, *33*) has immense potential for broader applications beyond the field of boiling. It could be adapted to study steam (*65*) or refrigerant (*66*) condensation during two-phase flows, corrosion (*67*), and erosion mechanisms in high or low *Re* single-phase flows (*68*), flow fouling dynamics (*69*), chemical (*70*) or biomolecular (*71*) processes undergoing transition during flow, or distillation and separation processes. This versatility expands the scope and impact of our work, making it applicable to a wide range of flow scenarios.

In summary, in this work, we developed a powerful boroscopy method to study the unique microscale bubble and flow regime physics. This enabled direct in situ and in-liquid visual observations that, alongside thermodynamic and heat transfer analysis and surface characterization, shed light on the mechanisms governing surface structure enhanced flow boiling. The results showed that the HTC can be notably enhanced with the use of etched surface structures when compared to plain surfaces. Boroscopy elucidated that etched surfaces result in a higher bubble nucleation density. The higher observed HTC enhancement for etched Al versus plain Al, when compared to etched Cu versus plain Cu, was found to be consistent with the higher bubble nucleation density on the etched Al surface. On the basis of the observed bubble dynamics, we show that the main force driving the differences between plain and etched surfaces is the unsteady drag force driven by the differences in wall superheat. Using mercury porosimetry, we show that the observed variations in the enhancement for the structured Al and Cu surfaces are due to the differences in their ability to match the optimal pore/cavity size range for flow boiling and surfaces with multitudinous large and active cavities such as etched Al can offer a better heat transfer performance. The boroscopy method was used to show that the actual quality is higher on the etched surfaces, induced by enhanced nucleation that reduced thermal nonequilibrium. It was also shown that the transition to annular flow was generally delayed with structured surfaces, indicating the persistence of nucleate boiling at higher heat fluxes. It was also shown that an increase in actual quality and thus void fraction further thins the liquid film, worsens interface stability, and counters capillary effects, leading to no substantial dryout delay. Overall, our work provides valuable insights into the fundamentals of two-phase flow boiling heat transfer enhancement enabled by surface structuring using in situ boroscopy. Furthermore, our developed method has utility for a plethora of relevant applications and scientific domains where in-tube and in-channel observation is key to understanding the mechanisms of thermal, hydrodynamic, and chemical processes.

Downloaded from https://www.science.org at EPF Lausanne on October 12, 2025

MATERIALS AND METHODS

Surface preparation

Commercially available 1-m-long 1/4″ Al and Cu tubes (outer diameter = 6.35 mm, inner diameter = 4.72 mm for Cu and inner diameter = 4.57 mm for Al) were used for this work. The tubes were cleaned before the etching process using acetone, isopropyl alcohol (IPA), deionized (DI) water, and IPA again and dried with nitrogen gas. The outer surface of both tubes was protected from etching with the Kapton tape to ensure a smooth outer surface. The Al tube was put in a plastic container filled with 2 M hydrochloric acid and kept for 15 min. The Cu tube was put in a plastic container filled with ferric chloride (32% by volume) and kept for 20 min. Both surfaces were cleaned with DI water after the etching process and dried with nitrogen gas. See text S1 for additional details. The increase in the tube diameter due to etching was 3.50 ± 0.82% for the etched Al tube and 0.92 ± 0.20% for the etched Cu when compared to the corresponding plain tubes. See text S13 and fig. S16.

Heat transfer experiments

Figure 2A represents the experimental facility. Details of the setup operation are given in text S14 and fig. S17. In general, following Fig. 2A, the refrigerant (R515B, a low GWP, low ODP replacement for typical R134a) gets heated in the preheater, exits as a saturated liquid, and enters the test section. On the test section, 12 thermocouples at $z = 0.02$, 0.1, 0.3, 0.5, 0.7, and 0.95 m, both on top and bottom (6 each) azimuthal locations on the tube, are located as depicted in Fig. 2A. The first ($z = 0.02$ m), third ($z = 0.3$ m), and the last ($z = 0.95$ m) thermocouple locations are chosen to be the spots where the borescope was inserted to investigate the wall superheat and HTC at those very spots. The exit thermodynamic equilibrium quality was chosen as the metric to be kept the same for different cases. This ensures a consistent condition for comparative analysis of bubble dynamics, flow regime transitions, and dryout dynamics for different tubes and mass fluxes. Mathematically, with different permutations of mass flux (G) and diameter D, we change the heat flux (q'') to keep the exit thermodynamic equilibrium quality the same as per the equation $x_{e,out} = (4q''/Gh_{fg})(L/D)$. Since the equation is linear, as we keep the exit thermodynamic equilibrium quality the same, the local thermodynamic equilibrium qualities will be also kept the same at corresponding locations for different operational cases by changing L with z in the aforementioned equation $[x_{e,z} = (4q''/Gh_{fg})(z/D)]$. The temperatures are read by the thermocouples, while the flow is heated by the rope heater in small increments to reach the targeted exit thermodynamic equilibrium qualities ($x_{e,out} = 0.1$, 0.15, 0.2, 0.25, 0.30, 0.35, 0.4, 0.50, 0.60, 0.7, 0.8, and to dryout). The experiments were carried out at 800 kPa as the working pressure and at three different mass fluxes of $G = 100$, 150, and 200 kg/(m^2·s) in a heat flux range of $q'' = 0$ to 35 kW/m^2 for Al and at the mass flux of $G = 150$ kg/(m^2·s) and in a heat flux range of $q'' = 0$ to 25 kW/m^2 for Cu. Additional details for data validation, analysis, and uncertainty propagation are presented in texts S15 and S16, table S3, and table S4.

Boroscopy experiments

Three sets of boroscopy experiments were carried out to study different flow regimes of bubbly, slug, and annular flow by inserting the borescope at different locations of $z = 0.02$, 0.3, and 0.95 m. To study the two latter flow regimes, a Hawkeye Pro Hardy Gradient Lens Inc. borescope (outer diameter = 6.35 mm, 50°/~1.6-mm field of view) was used. To insert this borescope into the tube, an oval notch was drilled into the tubes. A 1/4″ brass tee junction fitting with plastic ferrules (to prevent the borescope from being plastically deformed) was used for the purpose of sealing as represented in Fig. 2C.

Because of the small size of bubbles on the etched Al, which were harder to capture with the Pro Hardy borescope, we used a Hawkeye MicroSlim (outer diameter = 1.85 mm, 40°/~0.96-mm field of view) that allowed for more detailed imaging of the bubble dynamics near the entrance. The higher magnification of this borescope provided a more detailed and clearer image of the ongoing bubble dynamics in the bubbly flow regime. To insert the borescope into the tube, a secondary rod was welded to the original tube (as shown in Fig. 2B), and a hole of 1.87 mm was drilled into the rod. Because of the extremely fine diameter of the borescope, standard fittings could not be used for sealing purposes. Therefore, a secondary rod around 70% of the length of the borescope probe was installed on the borescope and sealed with epoxy (Loctite 1C Hysol). The borescope was then inserted into the tube passing the welded tube, and the borescope and welded tube rod were connected and sealed using a Yor-Lok compression fitting. Please note that only the finer original rod of the borescope (outer diameter: 1.85 mm) is inserted into the testing tube. By using this approach, a comprehensive and detailed analysis of the bubble behavior near the tube inlet was made possible by gaining a higher level of accuracy (finer pixel size) in the observations and data collection. Further elaboration on the data processing is provided in text S17.

Supplementary Materials

The PDF file includes:

Supplementary Text S1 to S17
Figs. S1 to S17
Tables S1 to S4
Legend for movies S1 to S5
References

Other Supplementary Material for this manuscript includes the following:

Movies S1 to S5

REFERENCES AND NOTES

1. D. Agonafer, M. S. Spector, N. Miljkovic, Materials and interface challenges in high vapor quality two-phase flow boiling research. *IEEE Trans. Compon. Packaging Manuf. Technol.* **11**, 1583–1591 (2021).
2. Y. Huang, Q. Yang, J. Zhao, J. Miao, X. Shen, W. Fu, Q. Wu, Y. Guo, Experimental study on flow boiling heat transfer characteristics of ammonia in microchannels. *Microgravity Sci. Technol.* **32**, 477–492 (2020).
3. M. H. Mousa, C. M. Yang, K. Nawaz, N. Miljkovic, Review of heat transfer enhancement techniques in two-phase flows for highly efficient and sustainable cooling. *Renew. Sustain. Energy Rev.* **155**, 111896 (2022).
4. J. M. Beér, High efficiency electric power generation: The environmental role. *Prog. Energy Combust. Sci.* **33**, 107–134 (2007).
5. W. L. Johnson, J. R. Stephens, NASA's cryogenic fluid management technology development roadmaps. No. GRC-E-DAA-TN60252. (2018).
6. V. Ganesan, R. Patel, J. Hartwig, I. Mudawar, Universal critical heat flux (CHF) correlations for cryogenic flow boiling in uniformly heated tubes. *Int. J. Heat Mass Transf.* **166**, 120678 (2021).
7. G. Liang, I. Mudawar, Review of channel flow boiling enhancement by surface modification, and instability suppression schemes. *Int. J. Heat Mass Transf.* **146**, 118864 (2020).
8. Y. Zhu, D. S. Antao, K. H. Chu, S. Chen, T. J. Hendricks, T. Zhang, E. N. Wang, Surface structure enhanced microchannel flow boiling. *J. Heat Transfer* **138**, 091501 (2016).
9. K. Luo, W. Li, J. Ma, W. Chang, G. Huang, C. Li, Silicon microchannels flow boiling enhanced via microporous decorated sidewalls. *Int. J. Heat Mass Transf.* **191**, 122817 (2022).
10. L. Wang, X. Luo, J. Zhang, B. He, Z. Peng, Flow boiling characteristics of minichannel heat sink with artificial conical cavities array under electric field. *Int. J. Heat Mass Transf.* **173**, 121286 (2021).

Downloaded from https://www.science.org at EPF Lausanne on October 12, 2025

11. A. K. M. M. Morshed, F. Yang, M. Y. Ali, J. A. Khan, C. Li, Enhanced flow boiling in a microchannel with integration of nanowires. *Appl. Therm. Eng.* **32**, 68–75 (2012).
12. W. Chang, W. Li, J. Ma, K. Luo, C. Li, Enhanced flow boiling in microchannels integrated with hierarchical structures of micro-pinfin fences and nanowires. *Langmuir* **37**, 8989–8996 (2021).
13. D. P. Ghosh, D. Sharma, D. Mohanty, S. K. Saha, R. Raj, Facile fabrication of nanostructured microchannels for flow boiling heat transfer enhancement. *Heat Transf. Eng.* **40**, 537–548 (2019).
14. V. Khanikar, I. Mudawar, T. Fisher, Effects of carbon nanotube coating on flow boiling in a micro-channel. *Int. J. Heat Mass Transf.* **52**, 3805–3817 (2009).
15. C. S. S. Kumar, S. Suresh, L. Yang, Q. Yang, S. Aravind, Flow boiling heat transfer enhancement using carbon nanotube coatings. *Appl. Therm. Eng.* **65**, 166–175 (2014).
16. N. Singh, V. Sathyamurthy, W. Peterson, J. Arendt, D. Banerjee, Flow boiling enhancement on a horizontal heater using carbon nanotube coatings. *Int. J. Heat Fluid Flow* **31**, 201–207 (2010).
17. S. Huang, L. Wang, Z. Pan, Z. Zhou, Experimental investigation of a new hybrid structured surface for subcooled flow boiling heat transfer enhancement. *Appl. Therm. Eng.* **192**, 116929 (2021).
18. N. V. Upot, K. F. Rabbi, A. Bakhshi, J. Kohler Mendizabal, A. M. Jacobi, N. Miljkovic, Etching-enabled ultra-scalable micro and nanosculpturing of metal surfaces for enhanced thermal performance. *Appl. Phys. Lett.* **122**, 031603 (2023).
19. M. Shojaeian, A. Koşar, Pool boiling and flow boiling on micro- and nanostructured surfaces. *Exp. Therm. Fluid Sci.* **63**, 45–73 (2015).
20. H. S. Ahn, M. H. Kim, A review on critical heat flux enhancement with nanofluids and surface modification. *J. Heat Transfer* **134**, 024001 (2012).
21. K. C. Leong, J. Y. Ho, K. K. Wong, A critical review of pool and flow boiling heat transfer of dielectric fluids on enhanced surfaces. *Appl. Therm. Eng.* **112**, 999–1019 (2017).
22. V. Ganesan, M. J. Inanlu, N. Miljkovic, High-fidelity model to predict heat transfer enhancement for liquid film boiling on uniform micro-structured wicking surfaces. *Natl. Sci. Rev.* **11**, nwae148 (2024).
23. Z. Wu, B. Sundén, On further enhancement of single-phase and flow boiling heat transfer in micro/minichannels. *Renew. Sustain. Energy Rev.* **40**, 11–27 (2014).
24. G. Liang, I. Mudawar, Review of nanoscale boiling enhancement techniques and proposed systematic testing strategy to ensure cooling reliability and repeatability. *Appl. Therm. Eng.* **184**, 115982 (2021).
25. N. V. Upot, K. F. Rabbi, S. Khodakarami, J. Y. Ho, J. K. Mendizabal, N. Miljkovic, Advances in micro and nanoengineered surfaces for enhancing boiling and condensation heat transfer: A review. *Nanoscale Adv.* **5**, 1232–1270 (2023).
26. D. E. Kim, D. I. Yu, D. W. Jerng, M. H. Kim, H. S. Ahn, Review of boiling heat transfer enhancement on micro/nanostructured surfaces. *Exp. Therm. Fluid Sci.* **66**, 173–196 (2015).
27. H. Chu, X. Yu, H. Jiang, D. Wang, N. Xu, Progress in enhanced pool boiling heat transfer on macro-and micro-structured surfaces. *Int. J. Heat Mass Transf.* **200**, 123530 (2023).
28. P. Sen, S. Kalita, D. Sen, A. K. Das, B. B. Saha, Pool boiling heat transfer and bubble dynamics of modified copper micro-structured surfaces. *Int. Commun. Heat Mass Transf.* **134**, 106039 (2022).
29. C. A. Chen, K. W. Li, T. F. Lin, W. K. Li, W. M. Yan, Study on heat transfer and bubble behavior inside horizontal annuli: Experimental comparison of R-134a, R-407C, and R-410A subcooled flow boiling. *Case Stud. Therm. Eng.* **24**, 100875 (2021).
30. T. Dong, Z. Yang, Q. Bi, Y. Zhang, Freon R141b flow boiling in silicon microchannel heat sinks: Experimental investigation. *Heat Mass Transf.* **44**, 315–324 (2008).
31. M. W. Sulaiman, C.- C. Wang, Effect of contraction on the convective boiling heat transfer of microchannel heat sinks. *Appl. Therm. Eng.* **223**, 120026 (2023).
32. J. Li, D. Kang, K. F. Rabbi, W. Fu, X. Yan, X. Fang, L. Fan, N. Miljkovic, Liquid film-induced critical heat flux enhancement on structured surfaces. *Sci. Adv.* **7**, eabg4537 (2021).
33. J. Li, G. Zhu, D. Kang, W. Fu, Y. Zhao, N. Miljkovic, Endoscopic visualization of contact line dynamics during pool boiling on capillary-activated copper microchannels. *Adv. Funct. Mater.* **31**, 2006249 (2021).
34. N. V. Upot, A. Bakhshi, K. F. Rabbi, F. Lu, A. M. Jacobi, N. Miljkovic, Enhanced refrigerant flow boiling heat transfer in microstructured finned surfaces. *Int. J. Heat Mass Transf.* **207**, 123999 (2023).
35. N. V. Upot, A. Mahvi, K. F. Rabbi, J. Li, A. M. Jacobi, N. Miljkovic, Scalable and resilient etched metallic micro- and nanostructured surfaces for enhanced flow boiling. *ACS Appl. Nano Mater.* **4**, 6648–6658 (2021).
36. J. K. Mendizábal, B. P. Singh, K. F. Rabbi, N. V. Upot, K. Nawaz, A. Jacobi, N. Miljkovic, Enhanced internal condensation of R1233zd (E) on micro-and nanostructured copper and aluminum surfaces. *Int. J. Heat Mass Transf.* **207**, 124012 (2023).
37. W. Fu, Y. Chen, M. J. Inanlu, T. S. Thukral, J. Li, N. Miljkovic, Enhanced pool boiling of refrigerants R-134a, R-1336mzz(Z) and R-1336mzz(E) on micro-and nanostructured tubes. *Int. J. Heat Mass Transf.* **220**, 124983 (2024).
38. J. R. Thome, L. Consolini, *Mechanisms of Boiling in Microchannels: Critical Assessment in Microfluidics Based Microsystems*. NATO Science for Peace and Security Series A: Chemistry and Biology. S. Kakaç, B. Kosoy, D. Li, A. Pramuanjaroenkij, Eds. (Springer, Dordrecht, 2010).
39. W. Li, Y. Lin, K. Zhou, J. Li, J. Zhu, Local heat transfer of saturated flow boiling in vertical narrow microchannel. *Int. J. Therm. Sci.* **145**, 105996 (2019).
40. T. Alam, W. Li, W. Chang, F. Yang, J. Khan, C. Li, A comparative study of flow boiling HFE-7100 in silicon nanowire and plainwall microchannels. *Int. J. Heat Mass Transf.* **124**, 829–840 (2018).
41. J. J. Wei, H. Honda, Effects of fin geometry on boiling heat transfer from silicon chips with micro-pin-fins immersed in FC-72. *Int. J. Heat. Mass Transf.* **46**, 4059–4070 (2003).
42. J. F. Klausner, R. Mei, D. M. Bernhard, L. Z. Zeng, Vapor bubble departure in forced convection boiling. *Int. J. Heat Mass. Transf.* **36**, 651–662 (1993).
43. B. B. Mikic, W. M. Rohsenow, P. Griffith, On bubble growth rates. *Int. J Heat Mass Transf.* **13**, 657–666 (1970).
44. L. Z. Zeng, J. F. Klausner, D. M. Bernhard, R. Mei, A unified model for the prediction of bubble detachment diameters in boiling systems—II. Flow boiling. *Int. J. Heat Mass Transf.* **36**, 2271–2279 (1993).
45. C. Wang, O. Akinsulire, G. Su, B. Phillips, M. Rahman, M. Bucci, Enhancement of pressurized subcooled flow boiling chf with nano-engineered surfaces. *NURETH-18* **591**, 18–23 (2019).
46. A. R. Ali, R. L. Judd, An analytical and experimental investigation of bubble waiting time in nucleate boiling. *J. Heat Transf.* **103**, 673–678 (1981).
47. D. Sarker, W. Ding, R. Franz, O. Varlamova, P. Kovats, K. Zähringer, U. Hampel, Investigations on the effects of heater surface characteristics on the bubble waiting period during nucleate boiling at low subcooling. *Exp. Therm. Fluid Sci.* **101**, 76–86 (2019).
48. Y. Y. Hsu, On the size range of active nucleation cavities on a heating surface. *J. Heat Transf.* **84**, 207–213 (1962).
49. Y.- Y. Hsu, R. W. Graham, *An Analytical and Experimental Study of the Thermal Boundary Layer and Ebullition Cycle in Nucleate Boiling* (National Aeronautics and Space Administration, 594, 1961).
50. M. H. A. A. Mousa, "Liquid vapor phase change for highly efficient and sustainable cooling," thesis, University of Illinois Urbana-Champaign (2022).
51. H. J. Oh, J. H. Lee, H. J. Ahn, Y. Jeong, N. J. Park, S. S. Kim, C. S. Chi, Etching characteristics of high-purity aluminum in hydrochloric acid solutions. *Mater. Sci. Eng. A* **449**, 348–351 (2007).
52. W. H. Burrows, C. T. Lewis Jr., D. E. Saëre, R. E. Brooks, Kinetics of the copper-ferric chloride reaction and the effects of certain inhibitors. *Ind. Eng. Chem. Process Des. Dev.* **3**, 149–159 (1964).
53. V. Ganesan, R. Patel, J. Hartwig, I. Mudawar, Universal correlations for post-CHF saturated and superheated flow film boiling heat transfer coefficient, minimum heat flux and rewet temperature for cryogenic fluids in uniformly heated tubes. *Int. J. Heat Mass Transf.* **195**, 123054 (2022).
54. H. Li, P. S. Hrnjak, "Flow Visualization of R134a, R1234ze(E), and R1234yf in microchannel tube" in *International Refrigeration and Air Conditioning Conference* (2018).
55. B. Sumith, F. Kaminaga, K. Matsumura, Saturated flow boiling of water in a vertical small diameter tube. *Exp. Therm. Fluid Sci.* **27**, 789–801 (2003).
56. J. E. Galloway, I. Mudawar, CHF mechanism in flow boiling from a short heated wall—II. Theoretical CHF model. *Int. J. Heat Mass Transf.* **36**, 2527–2540 (1993).
57. X. Dai, F. Yang, R. Yang, Y.-C. Lee, C. Li, Micromembrane-enhanced capillary evaporation. *Int. J. Heat Mass Transf.* **64**, 1101–1108 (2013).
58. S. Szczukiewicz, M. Magnini, J. R. Thome, Proposed models, ongoing experiments, and latest numerical simulations of microchannel two-phase flow boiling. *Int. J. Multiph. Flow* **59**, 84–101 (2014).
59. M. Yazdani, T. Radcliff, M. Soteriou, A. A. Alahyari, A high-fidelity approach towards simulation of pool boiling. *Phys. Fluids* **28**, 012111 (2016).
60. S. Garimella, U. C. Andresen, B. Mitra, Y. Jiang, B. M. Fronk, Heat transfer during near-critical-pressure condensation of refrigerant blends. *J. Heat Transf.* **138**, 051503 (2016).
61. S. Garimella, B. Mitra, U. C. Andresen, Y. Jiang, B. M. Fronk, Heat transfer and pressure drop during supercritical cooling of HFC refrigerant blends. *Int. J. Heat Mass Transf.* **91**, 477–493 (2015).
62. S. Khodakarami, K. F. Rabbi, Y. Suh, Y. Won, N. Miljkovic, Machine learning enabled condensation heat transfer measurement. *Int. J. Heat Mass Transf.* **194**, 123016 (2022).
63. Y. He, C. Hu, B. Jiang, Z. Sun, J. Ma, H. Li, D. Tang, Data-driven approach to predict the flow boiling heat transfer coefficient of liquid hydrogen aviation fuel. *Fuel* **324**, 124778 (2022).
64. H. Bao, J. Feng, N. Dinh, H. Zhang, Deep learning interfacial momentum closures in coarse-mesh CFD two-phase flow simulation using validation data. *Int. J. Multiph. Flow* **135**, 103489 (2021).
65. H. Bian, Z. Sun, M. Ding, N. Zhang, Local phenomena analysis of steam condensation in the presence of air. *Prog. Nucl. Energy* **101**, 188–198 (2017).
66. L. Doretti, C. Zilio, S. Mancin, A. Cavallini, Condensation flow patterns inside plain and microfin tubes: A review. *Int. J. Refrig.* **36**, 567–587 (2013).

Downloaded from https://www.science.org at EPF Lausanne on October 12, 2025

67. A. A. Farag, E. A. Mohamed, A. Toghan, The new trends in corrosion control using superhydrophobic surfaces: A review. *Corrosion Rev.* **41**, 21–37 (2023).
68. Q. H. Mazumder, Prediction of erosion due to solid particle impact in single-phase and multiphase flows. *J. Press. Vessel Technol.* **129**, 576–582 (2007).
69. S. Hatte, R. Stoddard, R. Pitchumani, Generalized analysis of dynamic flow fouling on heat transfer surfaces. *Int. J. Heat Mass Transf.* **188**, 122573 (2022).
70. J. M. Ottino, Mixing and chemical reactions a tutorial. *Chem. Eng. Sci.* **49**, 4005–4027 (1994).
71. W. E. Arter, R. Qi, N. A. Erkamp, G. Krainer, K. Didi, T. J. Welsh, J. Acker, J. Nixon-Abell, S. Qamar, J. Guillén-Boixet, Biomolecular condensate phase diagrams with a combinatorial microdroplet platform. *Nat. Commun.* **13**, 7845 (2022).
72. J. W. Coleman, S. Garimella, Two-phase flow regimes in round, square and rectangular tubes during condensation of refrigerant R134a. *Int. J. Refrig.* **26**, 117–128 (2003).
73. J. Li, Y. Lin, K. Zhou, W. Li, Subcooled flow boiling on micro-porous structured copper surface in a vertical mini-gap channel. *J. Therm. Sci. Eng. Appl.* **12**, 061010 (2020).
74. V. Ganesan, R. Patel, J. Hartwig, I. Mudawar, Development of two-phase frictional pressure gradient correlation for saturated cryogenic flow boiling in uniformly heated tubes. *Int. J. Heat Mass Transf.* **220**, 124901 (2024).
75. V. Ganesan, R. Patel, J. Hartwig, I. Mudawar, Review of databases and correlations for saturated flow boiling heat transfer coefficient for cryogens in uniformly heated tubes, and development of new consolidated database and universal correlations. *Int. J. Heat Mass Transf.* **179**, 121656 (2021).
76. J. O. Hinze, *Turbulence* (McGraw-Hill, 1975).
77. L. V. Zysin, L. A. Fel'Dberg, A. L. Dobkes, A. G. Sazhenin, Allowance for optical distortion produced by temperature gradients in investigating the shape of vapor bubbles generated on a flat wall. *Heat Transfer, Sov. Res.* **12**, 6–10 (1980).
78. V. P. Carey, *Liquid-Vapor Phase-Change Phenomena: An Introduction to the Thermophysics of Vaporization and Condensation Processes in Heat Transfer Equipment* (CRC Press, 2020).
79. J. G. Collier, J. R. Thome, *Convective Boiling and Condensation* (Clarendon Press, 1994).
80. D. Taler, J. Taler, Simple heat transfer correlations for turbulent tube flow. *E3S Web Conf.* **13**, 02008 (2017).
81. A. J. Ghajar, S. M. Bhagwat, "Flow patterns, void fraction and pressure drop in gas-liquid two phase flow at different pipe orientations" in *Frontiers Progress in Multiphase Flow I* (Springer; 2014), pp. 157–212.
82. W. R. Lockhart, R. C. Martinelli, Proposed correlation of data for isothermal two-phase, two-component flow in pipes. *Chem. Eng. Prog.* **45**, 39–48 (1949).
83. A. Mukherjee, S. G. Kandlikar, Z. J. Edel, Numerical study of bubble growth and wall heat transfer during flow boiling in a microchannel. *Int J. Heat Mass Transf.* **54**, 3702–3718 (2011).

Acknowledgments: We thank R. T. Haasch at the Materials Research Laboratory at the University of Illinois for assistance in XPS characterizations and insightful discussions. **Funding:** We gratefully acknowledge funding support from the Office of Naval Research (ONR) under grant no. N00014-21-1-2089. N.M. also gratefully acknowledges funding support from the International Institute for Carbon Neutral Energy Research (WPI-I2CNER), sponsored by the Japanese Ministry of Education, Culture, Sports, Science and Technology. **Author contributions:** N.M. and J.L. collaboratively formulated the idea for this research. N.M. guided the work. N.V.U. built the heat transfer experimental facility. N.V.U., A.B., and W.F. guided the heat transfer data acquisition and analysis. J.L. guided the visualization experiments. K.F.R. and T.S.T. guided the surface preparation. M.J.I. and K.F.R. prepared the surfaces. M.J.I., Z.S., and V.B. carried out thermodynamic and visualization experiments. M.J.I., K.F.R., and P.K. characterized the structures. M.J.I. analyzed the thermodynamic data. Z.S. analyzed the visualization data. V.G., M.J.I., and C.W. carried out the theoretical analysis. M.J.I., V.G., C.W., and N.M. wrote the manuscript. **Competing interests:** The authors declare that they have no competing interests. **Data and materials availability:** All data needed to evaluate the conclusions in the paper are present in the paper and/or the Supplementary Materials.

Submitted 15 April 2024
Accepted 7 October 2024
Published 8 November 2024
10.1126/sciadv.adp8632

Downloaded from https://www.science.org at EPF Lausanne on October 12, 2025